

**TECHNICAL REPORT
NATICK/TR-05/011**



AD _____

BIOLOGICALLY-INSPIRED MICRO-ROBOTS:
Volume 2, Investigation of a Micro-Joint Angle Sensor
Using MEMS Cilia

by
Gary K. Fedder
and
Lauren Elizabeth de Rosset

Case Western Reserve University
Cleveland, OH 44106 - 7222

September 2005

Final Report
June 1998 – September 2002

Approved for public release; distribution is unlimited

Prepared for
U.S. Army Research, Development and Engineering Command
Natick Soldier Center
Natick, Massachusetts 01760-5020

REPORT DOCUMENTATION PAGE				Form Approved OMB No. 0704-0188																	
The public reporting burden for this collection of information is estimated to average 1 hour per response, including the time for reviewing instructions, searching existing data sources, gathering and maintaining the data needed, and completing and reviewing the collection of information. Send comments regarding this burden estimate or any other aspect of this collection of information, including suggestions for reducing the burden, to Department of Defense, Washington Headquarters Services, Directorate for Information Operations and Reports (0704-0188), 1215 Jefferson Davis Highway, Suite 1204, Arlington, VA 22202-4302. Respondents should be aware that notwithstanding any other provision of law, no person shall be subject to any penalty for failing to comply with a collection of information if it does not display a currently valid OMB control number.																					
PLEASE DO NOT RETURN YOUR FORM TO THE ABOVE ADDRESS.																					
1. REPORT DATE (DD-MM-YYYY) 15-09-2005		2. REPORT TYPE Final Report		3. DATES COVERED (From - To) June 1998 - September 2002																	
4. TITLE AND SUBTITLE BIOLOGICALLY-INSPIRED MICRO-ROBOTS: Volume 2, Investigation of a Micro-Joint Angle Sensor Using MEMS Cilia				5a. CONTRACT NUMBER C-DAAN02-98-C-4027																	
				5b. GRANT NUMBER																	
				5c. PROGRAM ELEMENT NUMBER																	
6. AUTHOR(S) Gary K. Fedder and Lauren Elizabeth de Rosset				5d. PROJECT NUMBER																	
				5e. TASK NUMBER																	
				5f. WORK UNIT NUMBER																	
7. PERFORMING ORGANIZATION NAME(S) AND ADDRESS(ES) Case Western Reserve University Mechanical Engineering Dept. 10900 Euclid Avenue Cleveland, OH 44106-7222				8. PERFORMING ORGANIZATION REPORT NUMBER																	
9. SPONSORING/MONITORING AGENCY NAME(S) AND ADDRESS(ES) Sponsor: Defense Advanced Research Projects Agency (DARPA) Microsystems Technology Office (Elana Ethridge) 3701 North Fairfax Drive Arlington, VA 22203-1714				10. SPONSOR/MONITOR'S ACRONYM(S)																	
				11. SPONSOR/MONITOR'S REPORT NUMBER(S) NATICK/TR-05/011																	
12. DISTRIBUTION/AVAILABILITY STATEMENT Approved for public release; distribution is unlimited.																					
13. SUPPLEMENTARY NOTES Monitor: US Army Research, Development & Engineering Command, Natick Soldier Center, ATTN: AMSRD-NSC-SS-MA (T. Gilroy), Kansas Street, Natick, MA 01760-5020																					
14. ABSTRACT This is one of three reports on the study of micro-robots. This document describes the design and fabrication of a joint angle sensor composed of an array of curled, directionally-sensitive microelectromechanical systems (MEMS) cantilever beams with piezoresistive sense elements, analogous to an insect hair plate. The sensor is to be embedded in the limb, such that the surface of the chip is flush with the surface of the limb. Actuation is then to be accomplished mechanically using a stylus that bends the hairs. An alternative actuation method is magnetic actuation. A layer of a hard magnetic material can be sputtered on the beams and magnetized. The beams would then be actuated with a permanent magnet. The magnetic actuation is preferable, as it is a non-contact solution. The polysilicon piezoresistors used to sense motion of the cilia have been tested, and using MemCAD software to obtain stress values, coefficients of piezoresistivity have been obtained for both Advanced Monolithic Systems (AMS) and Hewlett-Packard (HP) fabrication processes. A low-voltage rail-to-rail common-mode input, rail-to-rail output operational amplifier has been designed to amplify the output of the polysilicon wheatstone. A second report (NATICK/TR-05/010) focuses on robots based on crickets, and a third report (NATICK/TR-05/012) examines micro-robots on abstracted biological principles.																					
15. SUBJECT TERMS <table style="width: 100%; border: none;"> <tr> <td>ROBOTS</td> <td>EMBEDDING</td> <td>MICROVALVES</td> <td>DESIGN(ENGINEERING)</td> </tr> <tr> <td>JOINTS</td> <td>ACTUATORS</td> <td>PIEZORESISTORS</td> <td>TEST AND EVALUATION</td> </tr> <tr> <td>SENSORS</td> <td>MICROROBOT</td> <td>SENSING ELEMENTS</td> <td>BIOLOGICALLY INSPIRED</td> </tr> <tr> <td>ROBOTICS</td> <td>LOCOMOTION</td> <td>MICROELECTRONICS</td> <td>MICROELECTROMECHANICAL SYSTEMS</td> </tr> </table>						ROBOTS	EMBEDDING	MICROVALVES	DESIGN(ENGINEERING)	JOINTS	ACTUATORS	PIEZORESISTORS	TEST AND EVALUATION	SENSORS	MICROROBOT	SENSING ELEMENTS	BIOLOGICALLY INSPIRED	ROBOTICS	LOCOMOTION	MICROELECTRONICS	MICROELECTROMECHANICAL SYSTEMS
ROBOTS	EMBEDDING	MICROVALVES	DESIGN(ENGINEERING)																		
JOINTS	ACTUATORS	PIEZORESISTORS	TEST AND EVALUATION																		
SENSORS	MICROROBOT	SENSING ELEMENTS	BIOLOGICALLY INSPIRED																		
ROBOTICS	LOCOMOTION	MICROELECTRONICS	MICROELECTROMECHANICAL SYSTEMS																		
16. SECURITY CLASSIFICATION OF:			17. LIMITATION OF ABSTRACT	18. NUMBER OF PAGES	19a. NAME OF RESPONSIBLE PERSON																
a. REPORT	b. ABSTRACT	c. THIS PAGE			Thomas Gilroy																
U	U	U	SAR	46	19b. TELEPHONE NUMBER (Include area code) 508-233-5855																

TABLE OF CONTENTS

LIST OF FIGURES.....	v
LIST OF TABLES.....	vi
PREFACE	vii
SUMMARY	1
1. Introduction	2
1.1 Introduction	2
1.2 Micro-robot Specifications	3
1.3 Commercial Joint Angle Sensors	4
1.3.1 Introduction.....	4
1.3.2 Magnetic and Optical Encoders	5
1.3.3 Potentiometers.....	5
1.3.4 Linear Voltage Differential Transducers	5
1.3.5 Strain Gages	6
1.3.6 Summary	6
1.4 Insect Proprioception.....	7
1.4.1 Introduction.....	7
1.4.2 Campaniform Sensilla.....	7
1.4.3 Chordotonal Sensilla.....	7
1.4.4 Stretch Receptors	9
1.4.5 Hair Plates.....	10
1.4.6 Summary	11
1.5 MEMS Joint Angle Sensor.....	12
1.5.1 Integration of Robot and Sensor	12
1.5.2 Cantilever Beam Fabrication	12
1.5.3 Previous Cantilever Beam Sensing Methods.....	13
1.6 Summary.....	14
2. Joint Angle Sensor Design	15
2.1 Introduction	15
2.2 Theory of Operation	16
2.2.1 Introduction.....	16
2.2.2 Stress Analysis.....	16
2.2.3 Piezoresistivity and Polysilicon	19
2.2.4 Summary	20
2.3 Cantilever Beam Composition.....	20
2.4 Integrated Signal Conditioning.....	21
2.4.1 Introduction.....	21
2.4.2 Wheatstone Bridge.....	22
2.4.3 Multiplexing.....	22
2.4.4 Summing	25
2.4.5 Sample/Hold	27

CONTENTS (Cont'd)

2.4.6	Summary	27
2.5	Summary	28
3.	Experimentation	28
3.1	Introduction	28
3.2	Operational Amplifier.....	28
3.3	Cilia	30
4.	Discussion	32
4.1	Sources of Error.....	33
4.1.1	Resistor Mismatch	33
4.1.2	MemCAD Simulations.....	33
4.2	Comparison of 1 st Generation and 2 nd Generation.....	33
4.3	Future Work.....	33
5.	Conclusions	34
6.	Bibliography	35

LIST OF FIGURES

Figure 1. Conceptual Drawing of CWRU Robotic Cricket	2
Figure 2. Limb with Muscle and Spring.....	3
Figure 3. Dimensions of Limb [Units are in inches]	4
Figure 4. Diagram of a Cross-sectional.....	8
Figure 5. Diagram of a Chordotonal Sensillum.....	9
Figure 6. Diagram of a Stretch Receptor	10
Figure 7. Diagram of the Base of a Trichoid Sensillum.....	11
Figure 8. Illustration of a Hair Plate	11
Figure 9. Release Process Steps	13
Figure 10. SEM of the 1 st Generation Joint Angle Sensor (JAS)	15
Figure 11. SEM of Released MEMS Cilium (1 st Generation)	15
Figure 12. SEM of the 2 nd Generation JAS.....	15
Figure 13. SEM of Released MEMS Cilia (2 nd Generation)	15
Figure 14. Change in von Mises Stress [1 st generation].....	17
Figure 15. Layout of Cilia Anchor [1 st generation].....	17
Figure 16. Change in von Mises Stress [2 nd generation]	18
Figure 17. Layout of Cilia Anchor [2 nd generation]	18
Figure 18. Calculating Beam Curl	21
Figure 19. Schematic of Resistor Layout	22
Figure 20. Layout of Cilium with Pseudo-cilium	23
Figure 21. Decoder for 1 st Generation JAS	23
Figure 22. 1 st Generation JAS – Individually Addressed Cilium	24
Figure 23. Amplification Circuit for 1 st Generation JAS	24
Figure 24. Wheatstone Bridges with Preamplification and Voltage Offset Cancellation	25
Figure 25. Summing Circuit Schematic	26
Figure 26. Sample/Hold Circuit Diagram.....	27
Figure 27. Open Loop Transfer Curve for Operational Amplifier.....	29
Figure 28. Phase Plot from Hspice Simulation	29
Figure 29. Cilia Characterization – 1 st Generation JAS	31
Figure 30. Cilia Characterization – 2 nd Generation JAS	31

LIST OF TABLES

Table 1. Post-Processing Steps and Parameters	12
Table 2. Average Stress Values for 1 st and 2 nd Generation Beams	18
Table 3. Coefficients of Piezoresistivity for Silicon for n- and p-type { 100} wafers and Doping Levels below 10 ¹⁸ cm ⁻³	19
Table 4. Fractional Change in Resistivity for Sample Coefficients of Piezoresistivity	20
Table 5. Calculated Fractional Change in Resistivity	20
Table 6. Lengths and Out-of-Plane Displacements	21
Table 7. Power Consumption for Individual Analog Components of 1 st Generation.....	24
Table 8. 1 st Generation Pins and Functions.....	25
Table 9. Power Consumption for the 2 nd Generation	26
Table 10. 2 nd Generation Pins and Functions	27
Table 11. Power Consumption for the 3 rd Generation	27
Table 12. Characterization of the Operational Amplifier from Simulation	29
Table 13. Target and Resultant Parameters.....	30
Table 14. Longitudinal Coefficients of Piezoresistivity for AMS .6 μm and HP .5 μm CMOS Processes	32

PREFACE

This report outlines the research undertaken by Case Western Reserve University, Cleveland, OH, and Carnegie Mellon University, Pittsburgh, PA to develop micro-robots and the components needed to fabricate those micro-robots. Two types of robots, each 3 inches long, resulted from this work along with several important components. This report is presented in three volumes: The first volume describes the development of a robot based upon a cricket; the second volume describes the development of microelectromechanical systems (MEMS) joint angle sensors based upon cilia; the third volume describes another type of robot that can run faster than any other legged vehicle of its size, run over relatively large obstacles, and operate for several hours without a change of batteries. The purpose of this report is to communicate the design, implementation and evaluation of these unique micro-robots and their essential components. The project was completed during the period June 1998 to September 2002 under contract number C-DAAN02-98-C-4027, under the direction of U.S. Army Research, Development and Engineering Command, Natick Soldier Center, Natick, MA, and sponsorship of the Defense Advanced Research Projects Agency (DARPA), Arlington, VA.

This report is one of a series of three. The references for the other reports are:

Quinn, R., Ritzmann, R., Phillips, S., Beer, R., Garverick, S., and Birch, M. (2005) *Biologically-Inspired Micro-Robots: Vol. 1, Robots Based on Crickets*, Technical Report, (NATICK/TR-05/010), U.S. Army Research, Development and Engineering Command (RDECOM), Natick Soldier Center, Natick, MA 01760.

Quinn, R., Ritzmann, R., Morrey, J., and Horchler, A. (2005) *Biologically-Inspired Micro-Robots: Vol. 3, Micro-Robot Based on Abstracted Biological Principles*, Technical Report, (NATICK/TR-05/012), U.S. Army Research, Development and Engineering Command (RDECOM), Natick Soldier Center, Natick, MA 01760.

BIOLOGICALLY INSPIRED MICRO-ROBOTS

Volume 2, Investigation of a Micro-Joint Angle Sensor Using Microelectromechanical Systems (MEMS) Cilia

SUMMARY

This is the second of three volumes describing the work performed in the Biologically Inspired Micro-Robots project. The overall goal of the project was to develop legged vehicles that can run and jump and that can fit in a 2-inch cube. Many technologies needed to be advanced in order for this project to succeed. Volume 1 describes the development of several of those technologies such as actuators, compressors, valves, and leg and robot designs. Other necessary components are joint angle sensors for closed loop control of the micro-robot's joint movements. Sensors of suitable miniature size and power requirements were not available for a legged micro-robot at the start of this project. In this volume the development of joint angle sensors for micro legged robots using MEMS fabrication processes are described. Volume 3 describes the development of micro robots that can run and jump based upon more abstracted biological principles.

This report (Volume 2) describes the design and fabrication of a joint angle sensor composed of an array of curled, directionally sensitive MEMS cantilever beams with piezoresistive sense elements, analogous to an insect hair plate. The sensor is to be embedded in the limb such that the surface of the chip is flush with the surface of the limb. Actuation is then to be accomplished mechanically using a stylus that bends the hairs. An alternative actuation method is magnetic actuation. A layer of a hard magnetic material can be sputtered on the beams and magnetized. The beams would then be actuated with a permanent magnet. The magnetic actuation is preferable, as it is a non-contact solution. The polysilicon piezoresistors used to sense motion of the cilia have been tested; and using MemCAD to obtain stress values, coefficients of piezoresistivity have been obtained for both AMS and HP fabrication processes. A low-voltage rail-to-rail common-mode input, rail-to-rail output operational amplifier has been designed to amplify the output of the polysilicon wheatstone. The operational amplifier performs closely to target parameters except for greater quiescent current consumption. Further iterations of the design need to be done to remove layout wiring errors to complete full system testing.

1. INTRODUCTION

1.1 Introduction

Biorobotics is the field of study that uses biological systems as models to develop artificial systems. The primary advantage to biorobotics is it learns from structures and designs that have been effectively used and developed over millions of years. A biological model of particular interest is cilia, which are microscopic hair-like structures. They function in numerous roles from hearing to locomotion in a multitude of species. With the advent of microelectromechanical systems (MEMS) technology, the manufacturing of such structures without scaling has become feasible.

Case Western Reserve University's (CWRU) development of a micro-autonomous vehicle based on the anatomy and physiology of a cricket provided the opportunity to investigate the production of synthetic cilia. Figure 1 shows a conceptual drawing of the robotic cricket with major sub-components labeled. The sub-component of interest to this project is the joint angle sensor required for controlled motion. Using biological models, MEMS cilia have been designed and fabricated to produce synthetic hair plates for joint angle sensing.

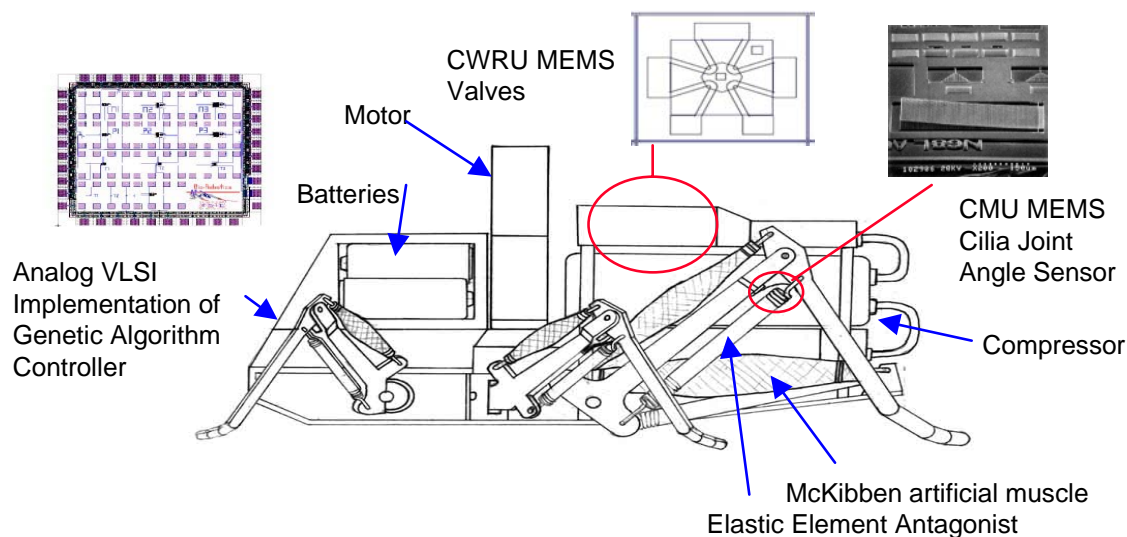


Figure 1. Conceptual Drawing of CWRU Robotic Cricket¹

In the first section of this document, specifications of the joint angle sensor will be discussed. Next, a review of commercial angle sensors will be done to determine if conventional technology will provide a suitable joint angle sensor. Insect physiology will then be reviewed in context of microelectromechanical systems (MEMS) fabrication; and concludes with a consideration of a MEMS implementation of a joint angle sensor. The second section will cover the sensor design and theory of operation, the third will contain

experimental results, the fourth contains a discussion, and the fifth summarizes the conclusion.

1.2 Micro-robot Specifications

As in a real cricket, the robotic cricket is propelled by six actuated limbs. The robot has several modes of motion: hopping, walking, and jumping. Each leg has at most two joints, and each joint requires a joint angle sensor for a minimum total of 12 sensors.

Movement of the limbs of the robot cricket is accomplished through the interaction of a spring and a muscle. Figure 2 illustrates the muscle/spring configuration. The muscle, called a McKibben artificial muscle, is a composite structure of a pneumatic balloon and a braided textile sleeve. Compressed air is used to inflate the balloon. The expansion of the balloon causes the contraction of the textile sleeve, which extends the limb. In advanced designs, the tension spring illustrated in Figure 2 is replaced by a torsional spring at the joint, which opens up the inner surface of the limb for placement of the joint angle sensor.

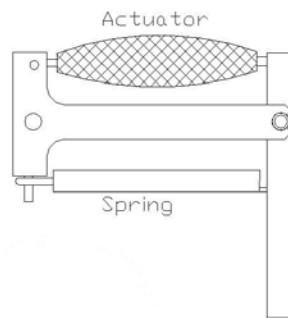


Figure 2. Limb with Muscle and Spring¹

The total robot is designed to fit into a 2"x2"x2" enclosure. By embedding the joint angle sensor in the limb of the cricket, increasing the size of the robot is avoided.

Inspection of

Figure 3 shows critical feature dimensions of length, width, and depth of the proximal portion of the limb where the sensor will be embedded. The available length is less than .9118", the width is .2", and the depth is .0938". In millimeters, these dimensions are 23.2 mm, 5.1 mm, and 2.4 mm, respectively.

The robotic cricket needs a single, continuous output per sensor that corresponds to a measurement of joint angle. The sensor signal requirement and the small size of the robot lead us to an approach where the necessary signal conditioning is integrated with the transduction elements. Also, the autonomous nature of the robot and the number of sensors required make minimizing power consumption desirable.

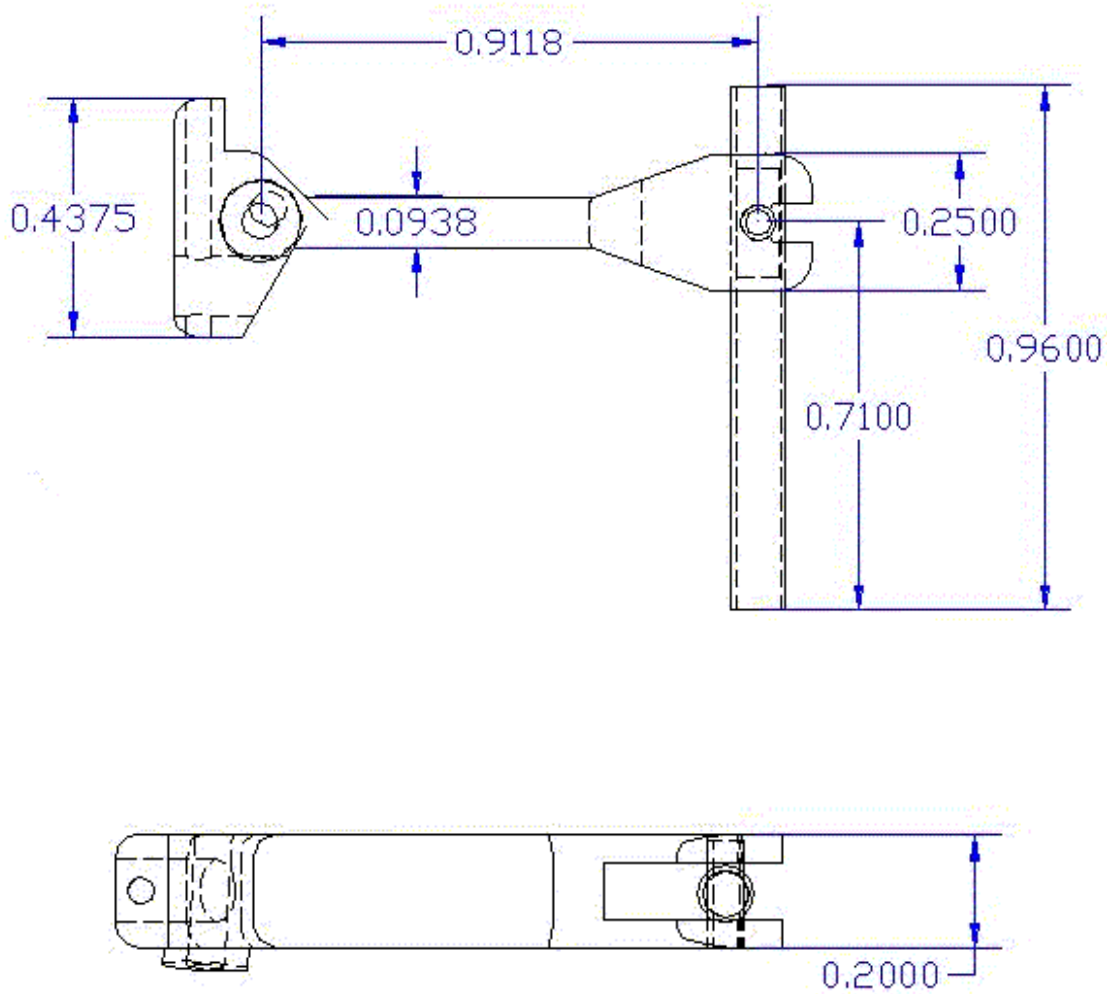


Figure 3. Dimensions of Limb¹ [Units are in inches]

1.3 Commercial Joint Angle Sensors

1.3.1 Introduction

A suitable commercial joint angle sensor would be the ideal solution. Commercial joint angle sensors are available and include, but are not limited to, encoders, potentiometers, linear differential voltage transducers (LDVT), and strain gages. Features of interest besides power and size are insensitivity to temperature, range, and resolution.

1.3.2 Magnetic and Optical Encoders

Optical encoders have three main components: a light source, a slotted wheel called a codewheel, and a light detector. The codewheel is connected to a shaft. As the wheel rotates with the shaft, the light path to the detector is periodically blocked and not blocked by the slots in the wheel. Light detection indicates a specific amount of rotational travel. Resolution for optical encoders, while limited by the number of slots per rotational length, is excellent and rotational travel is the full 360°. Interference by stray electrical and magnetic fields is not a concern, nor is this method sensitive to temperature. The dimensions for the smallest optical encoder from MicroMo, Inc. are 1.618"(41.1 mm)x1.181"(30.0 mm)x.72"(18.3 mm).²

Magnetic encoders also use code wheels. Instead of slots, the wheel has magnetic domains on its surface. Hall effect sensors detect the passing of the domains by the change in flux density. The resolution is comparable to optical encoders at 512 cpr (counts per revolution). The smallest magnetic encoder found is manufactured by MicroMo, Inc. The dimensions for the magnetic encoder are a diameter of .453"(13.3 mm) and a depth of .094"(2.4 mm).²

In order to use an optical or magnetic encoder, the largest viable diameter would be .25"(6.35 mm). Therefore, existing commercial the magnetic and optical encoders too large for this application.

1.3.3 Potentiometers

Rotary potentiometers are mechanical assemblies with three main components: a shaft, a circular resistive element (typically a carbon thin film or wire coil), and a mechanical arm (or brush). The two contacts of the resistor are the mechanical arm and one end of the resistive element. The mechanical arm is dragged along the surface of the carbon thin film; thus increasing or decreasing the resistance between the two contacts based on the effective length of the carbon thin film. Rotation of the mechanical arm is accomplished by attaching the potentiometer shaft to the rotating shaft. Potentiometers also can have nearly 360° of angle detection. Trimming potentiometers were the smallest rotary potentiometers found. They are available in a number of resistances from 1k to 1M. The Series 3364 Single-Turn Trimmer from Bourns has the smallest dimensions with a diameter at .157"(4 mm) and width of .059"(1.50 mm)³. However, these trimmers are not meant for continuous use and the rotational life is rated at 200 cycles. Therefore, potentiometers do not have the life times required for this application.

1.3.4 Linear Voltage Differential Transducers

A Linear Differential Voltage Transducer (LDVT) is a coil with a slidable aluminum or copper core. Voltage across the coil is proportional to the position of the core. By driving the coil with an AC current source and using predetection filtering of the output signal, a high rejection of interference from external fields is achieved.⁴ A commercial LDVT with the necessary dimensions is unavailable, however.

1.3.5 Strain Gages

There are several types of strain gages including mechanical, optical, and electrical. Mechanical gages and optical gages are unsuitable due to their size and delicacy, respectively. Successful electrical strain gages utilize the proportionality of resistance to strain. Such devices are piezoresistive or semiconductor, carbon-resistive, bonded metallic wire, and foil resistance. Carbon-resistive gages are highly susceptible to moisture and temperature. Piezoresistive strain gages are non-linear and temperature sensitive. However, with computer processing many of these defects can be neutralized. The positive features of piezoresistive strain gages are their high nominal resistance despite their small physical size, high sensitivity, and ability to measure both static and dynamics strains. Strain gages are suitable for the given task by size requirements. Monocrystalline silicon has a high coefficient of piezoresistivity. Polysilicon can, under specific conditions, have 60 to 70% of the sensitivity of monocrystalline silicon; and, it is a material available in conventional CMOS processes.⁵ For these reasons, polysilicon piezoresistive strain gages are utilized as the sensing elements in the MEMS cilia. A note of importance, though, is that strain gages are for measuring micro-strains. Piezoresistive strain gages are not capable of measuring large strains. They are liable to break under such conditions.

1.3.6 Summary

As most applications do not require such small dimensions, it is unsurprising that extremely small-scale LVDTs and encoders are not commercially available. However, while these joint angle sensors are unsuitable in their present commercial form, the benefits of these methods of operation promote investigation into their scalability and application to the CWRU cricket.

Optical encoders, potentiometers, and LVDTs are mechanical assemblies. It is conceivable that parts of the required size can be manufactured and assembled. With potentiometers, however, as the size of the resistive element is decreased the lifetime of the potentiometer is dramatically decreased due to the increased wear of the brush on the resistive element. LVDT quality also suffers with decreasing the physical size especially in regard to temperature sensitivity. Increasing temperature causes inductance and gain to increase. This effect is normally compensated in commercial LVDTs by increasing the core diameter, which is not an option in this case. In comparison, the LVDT is preferable to the potentiometer due to location on the robotic cricket. An LVDT could be embedded in the limb of the cricket, and joint motion could control the slidable core. Optical encoders are not nearly as susceptible to temperature as LVDTs and potentiometers, nor does the scaling of size significantly compromise the quality other than decreasing the resolution. The light must be focused, however, which requires lenses on either side of the encoder wheel. The alignment and placement of such lenses in the cricket leg would be extremely difficult. Such small scale would decrease allowable tolerances and vastly increase the difficulty of manufacturing and assembly, a failing of most mechanical assemblies. A magnetic encoder does not require a lens. Fixing a position device outside the joint places the device in a location prone to impact and damage, though. Therefore, its housing must support not only the cantilever load but

also the expected impacts. The necessary adjustments to the housing would increase the size and weight of the device, which is undesirable.

Another option is to find a one-component solution that can be embedded in the leg to avoid assembly and placement of multiple small parts on the joint. Strain gages, while temperature sensitive, are scalable. As the sensing elements in the MEMS cilia, the piezoresistive strain gages measure micro-strains as the cilia are mechanically deformed when the joint is actuated.

1.4 Insect Proprioception

1.4.1 Introduction

Proprioception is the ability to sense the position, movement, and orientation of the body.⁶ As the CWRU robotic cricket is modeled on actual cricket anatomy, an inspection of insect physiology with respect to proprioception might prove beneficial to MEMS JAS design. The four types of insect proprioceptors that are used for joint angle sensing are campaniform sensilla, stretch receptors, chordotonal sensilla, and hair plates (also called hair beds).^{7,8,9}

1.4.2 Campaniform Sensilla

The campaniform sensillum is a cuticular organ used to sense shearing stress. It is a thin, domed portion of the cuticle, oval in shape that is innervated along its longer axis with the dendrite of a bipolar neuron.

See **Figure 4** for an illustration of the campaniform sensillum. As the cuticle experiences stress, the dome is either raised or lower based on the type of stress, compression or extension, respectively, which is then detected by the neuron. Campaniform sensilla occur in all stressed parts of the insect body surface and are concentrated at the joints. The advantages of the campaniform sensillum as a biological model for the MEMS JAS are that it is a non-contact solution and has a low profile, which will not significantly increase the size of the robot. The disadvantages are the fabrication and packaging issues, especially in regard to attaching the sensor to the surface of the robotic cricket such that the sensor experiences the shear stresses on the surface of the robotic cricket. In addition, the issue of translating shear stresses on the surface of the robotic cricket into a joint angle measurement must be resolved.

1.4.3 Chordotonal Sensilla

Chordotonal organs are groups of scolopidia; sub-cuticular cord-like structures attached to points on the body wall and used as stretch receptors. Chordotonal organs are used for auditory sensing in addition to proprioception. Figure 5 is a diagram of a chordotonal sensillum. In the diagram, the components of interest are S which is the sense cell, A which is the axon of the sense cell, and D which is the dendrite of the sense cell. In addition to sharing the disadvantages of an artificial campaniform sensillum, the development of an elastomeric MEMS sensor is beyond the scope of this project due to required materials and processes.

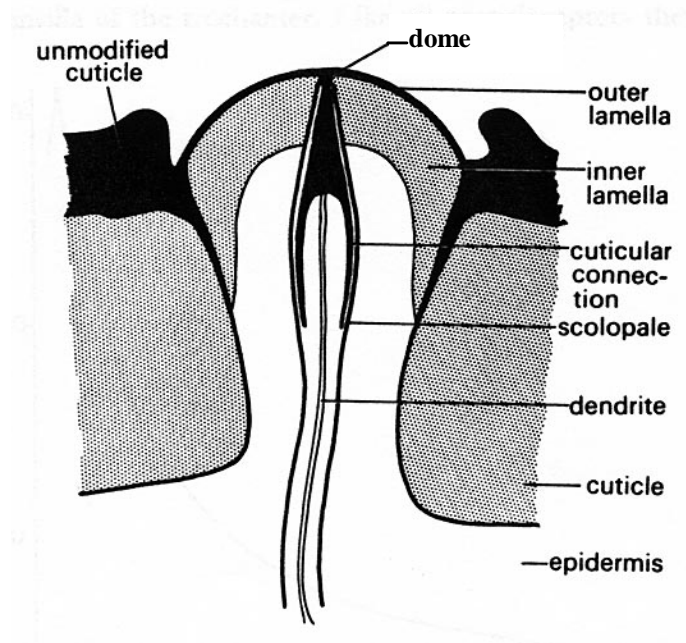


Figure 4. Diagram of a Cross-sectional View of a Campaniform Sensillum

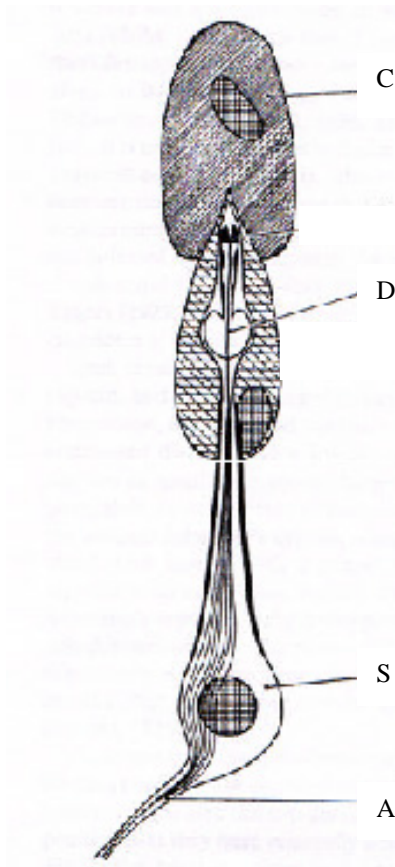


Figure 5. Diagram of a Chordotonal Sensillum

1.4.4 Stretch Receptors

Stretch receptors occur in three types of tissue: connective, muscle, and specialized muscle fibers and are shown in Figure 6. An artificial stretch receptor would innervate the McKibben artificial muscle. As with the chordotonal organ, however, the elastic nature of the organ prevents further study in this project.

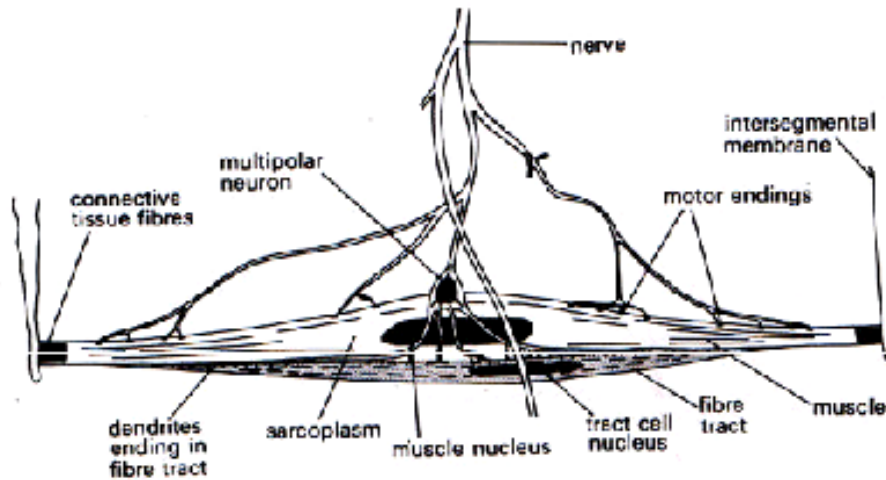


Figure 6. Diagram of a Stretch Receptor⁹

1.4.5 Hair Plates

Clusters of trichoid sensilla, hair-like projections of the cuticle, form the hair plates. Figure 7 is an illustration of a trichoid sensillum. The components of interest in the illustration are the tormagen cell, which produces the hair, and the trichogen cell, which produces the socket in which the hair is free to move. The nerve is composed of the axon and the dendrite. The nerve cell is activated by the mechanical deformation of the hair. The discharge of the neuron is proportional to the degree of bending experienced and often directionally sensitive. The stiff nature of the hair causes the force being transmitted to the base of the hair to be amplified much like a cantilever and a fulcrum.

While trichoid sensilla are used for multiple purposes and located on all surfaces, hair plates are used primarily for proprioception. The hair plates are stimulated by contact caused by intersegmental folding or adjoining surfaces upon joint motion. See Figure 8 for an illustration of intersegmental folding. In Figure 8, the coxa is the first segment of the leg of the insect joining the leg to the body, while the pleuron is the connecting body segment.

The fabrication of an artificial MEMS hair plate is possible if MEMS curled cantilever beams are used to mimic the trichoid sensillum. The similarities between the trichoid sensillum and the proposed MEMS cilia are that both are directionally sensitive and their responses are proportional to the degree of bending. Converting bending to a joint angle measurement is a less complex problem than converting shear stress to joint angle measurement. A significant difference between the two is that the MEMS cilia require more area as the beam is released from the surface of the sensor and the trichoid sensillum is grown normal to the surface. More discussion of MEMS curled cantilever beams and artificial hair plates follows in the next section.

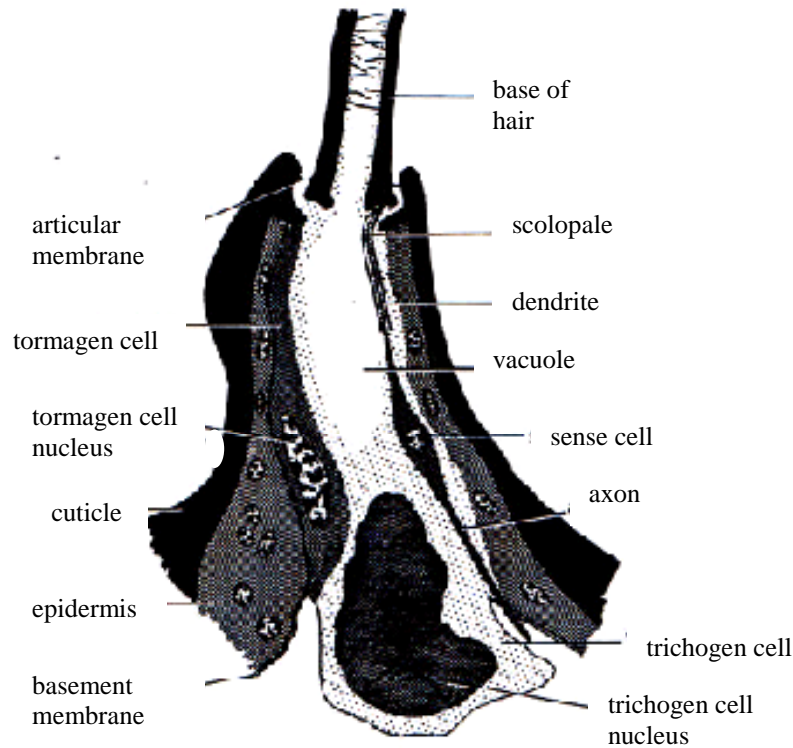


Figure 7. Diagram of the Base of a Trichoid Sensillum⁹



Figure 8. Illustration of a Hair Plate⁷

1.4.6 Summary

The outputs of all these biological sensors are integrated to form a complete picture of the insect's body parts and its orientation in the earth's gravitational field. To perfectly mimic a biological cricket, the CWRU robotic cricket would require a similar sensor fusion of several types of proprioceptors. Practical considerations prohibit this option for several reasons. First, designing and fabricating multiple types of sensors is expensive and time consuming. Second, computing power limits the amount of information capable of being integrated. Third, power and size constraints limit the number of sensors.

Fortunately, such complexity is not required for the CWRU robotic cricket as the joints of the cricket have at most two degrees of freedom. One type of sensor of small size and minimal power consumption at each joint should be able communicate enough information for the robot to function.

Any of the insect limb proprioceptors could be manufactured given enough time and the proper technology. From a feasibility standpoint within current MEMS technology, however, the options are limited. As standard integrated circuit microfabrication materials are thin, brittle and without large elastic components, implementation of a synthetic stretch receptor or synthetic chordotonal organ is not possible. A joint angle sensor inspired by campaniform sensilla might be possible perhaps with a MEMS diaphragm. However, it is the tactile hair-like trichoid sensilla that offer the greatest ease of implementation in the form of MEMS curled cantilever beams.

1.5 MEMS Joint Angle Sensor

1.5.1 Integration of Robot and Sensor

The joint angle sensor is composed of an array of curled, directionally sensitive MEMS cantilever beams with piezoresistive sense elements, analogous to an insect hair plate. The sensor will be embedded in the limb such that the surface of the chip is flush with the surface of the limb. Actuation will be accomplished mechanically using a stylus that bends the hairs. An alternative actuation method is magnetic actuation. A layer of a hard magnetic material can be sputtered on the beams and magnetized. The beams would then be actuated with a permanent magnet. The magnetic actuation is preferable, as it is a non-contact solution.

1.5.2 Cantilever Beam Fabrication

MEMS cantilever beams are fabricated using a standard CMOS process (Hewlett-Packard (HP) .5 μm 3-metal CMOS process) in conjunction with the CMU-MEMS post-CMOS process release.^{10,11} In this process, the top metal layer provides an etch resistant mask to post-processing release steps. The first step is to anisotropically etch exposed silicon dioxide. An isotropic etching step then removes the sacrificial silicon to release the structures. Due to the isotropic nature of the second step, circuits must be distanced from the etching boundaries by approximately 15 μm or they will be destroyed. The process steps and parameters are listed in Table 1 and illustrated in Figure 10.

Table 1. Post-Processing Steps and Parameters

	Anisotropic etch	Isotropic etch
Gas flow [sccm]	22.5 CHF ₃ 16 O ₂	150 SF ₆
Pressure [mT]	125	50
Power [W]	100	600 coil 12 platen
Etch rate [Å/min]	420	45,000

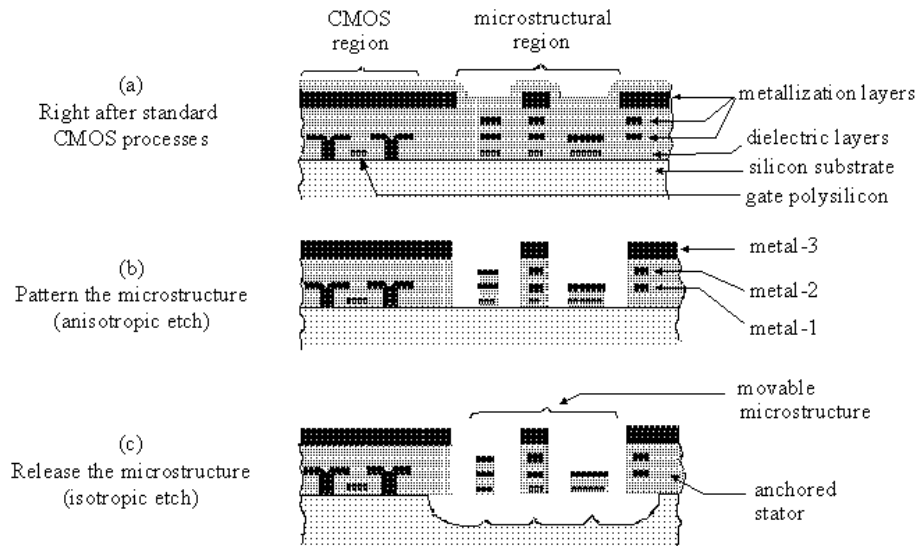


Figure 9. Release Process Steps¹¹

1.5.3 Previous Cantilever Beam Sensing Methods

1.5.3.1 Introduction

MEMS cantilever beams have been successfully used for multiple purposes from chemical sensing to vibration generation and detection. Of particular interest is the method with which the system detects stimuli. The sensing methods for previously fabricated cantilever beam devices are many, including electro-optical, piezoelectric, and piezoresistive.

1.5.3.2 Electro-optical

Electro-optical systems measure the modulation or intensity of light. Light transmission when produced off-chip is often achieved through optical fibers as in the case of a vibration sensor by E. Peiner et al.¹² In this case, a cantilever beam actuated by vibration is used to partially block the light path from transmitting to receiving fibers. Vibration is detected by measuring the intensity of light at the end of a receiving fiber. In another case of electro-optical detection applied to sensing, beam bending was monitored by

detecting the position of a point of light that was deflected by the apex of the beam.¹³ Changing interfacial stress caused beam bending. The specific chemicals attracted to the sensitized metal coatings on the beams changed interfacial stress when chemisorption or physisorption occurred. The benefits of an electro-optical detection strategy are high sensitivity and large tolerance of electromagnetic interference. In spite of these advantages, electro-optical strategies can include such high cost items as a laser, a collimator lens, among others, which require fine alignment and assembly.¹⁴

1.5.3.3 Piezoelectric

The piezoelectric effect is the electric polarization of charge when a piezoelectric material is stressed and also the mechanical deformation of a piezoelectric material when subjected to an applied voltage. Piezoelectric materials typically used in thin films are zinc oxide (ZnO) and single crystal lithium niobate (LiNbO₃).¹⁵ Instantiations of piezoelectric sensors were found in a microspeaker/microphone device¹⁶ and a tactile sensor.¹⁷ Both the microspeaker/microphone device and the tactile sensor were manufactured using a bulk micromachining process that sputters a layer of zinc oxide for the piezoelectric element. In the microspeaker/microphone, the one piezoelectric layer was used to actuate and detect vibration. In the tactile sensor, two layers were used, one for cantilever actuation and the other for detection. Another device that utilizes a piezoelectric cantilever beam is the atomic force microscope, which measures the topography of surfaces with high spatial resolution.^{18,19}

1.5.3.4 Piezoresistive

Piezoresistivity is the material property in which the bulk resistivity is altered by external mechanical stresses. Several devices such as an angular rate sensor²⁰ were found to use a piezoresistive-sensing element. The angular rate sensor uses a piezoresistor to detect vibrations caused by the driving force and the Coriolis force. Piezoresistors are typically fabricated by an ion implantation in a p-type wafer.

1.5.3.5 Summary

The ability of piezoelectric materials to both actuate and sense and the high sensitivity of electro-optics make both these strategies the ones that are most often used. These two strategies are inappropriate for several reasons, though. The size of the robotic and the necessary lenses preclude a conventional electro-optical solution, and piezoelectric materials are unavailable in the chosen process technology. However, piezoresistors are a viable alternative and can be manufactured using polysilicon.

1.6 Summary

The intention of this project is not to exactly reproduce an insect hair bed but to produce a viable joint angle sensor that operates on similar principles and is within the given dimensional and power constraints. However, the exploration of a MEMS implementation of a proven method such as the insect hair bed is worthwhile as cilia are used in many roles in biology from locomotion to sensing. If successfully imitated in MEMS technology, applications other than joint angle sensing might be addressed.

2. JOINT ANGLE SENSOR DESIGN

2.1 Introduction

Three versions of the MEMS joint angle sensor (JAS) were designed and fabricated. All share the basic architecture of an array of mechanically actuated cantilever beams with piezoresistive sensing elements embedded at the anchor of the beam. SEMs of the first two generations of ciliary joint angle sensors (JAS) are shown in Figure 10 through Figure 13.

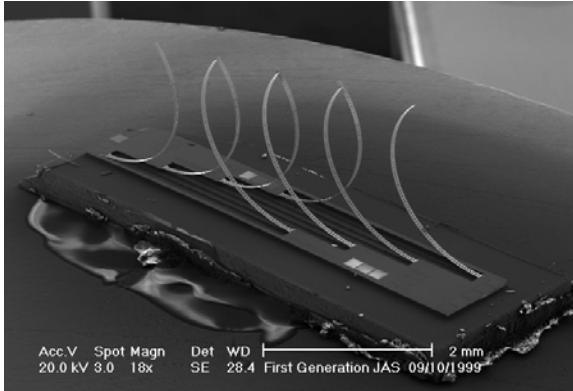


Figure 10. SEM of the 1st Generation Joint Angle Sensor (JAS)

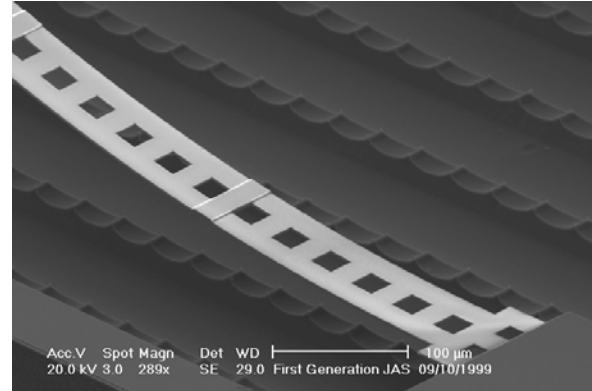


Figure 11. SEM of Released MEMS Cilium (1st Generation)

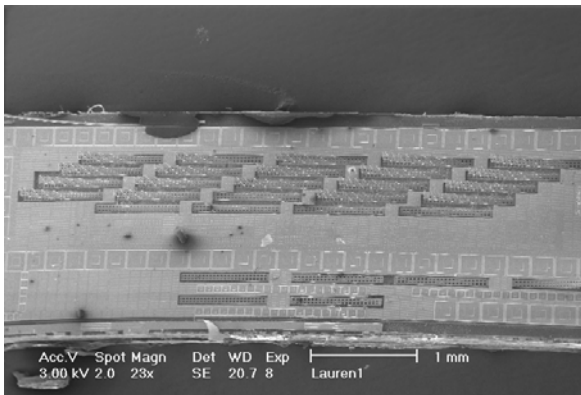


Figure 12. SEM of the 2nd Generation JAS

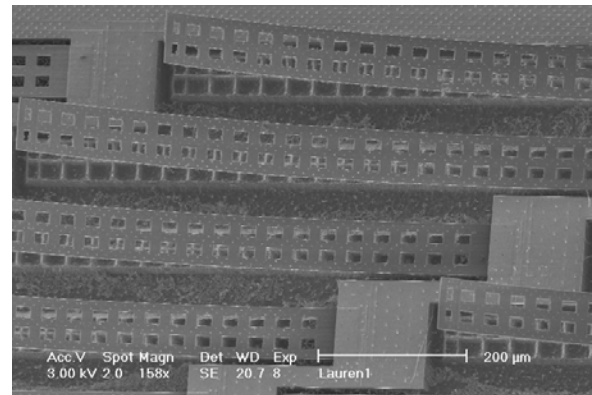


Figure 13. SEM of Released MEMS Cilia (2nd Generation)

Observing the sensor designs in the figures, several major differences can be noticed. First, while the overall size of the sensor is the same (1mm x 6mm), the length of the cilia are significantly different for the two generations (3 mm to .8 mm). This is due to a change in planned actuation method from mechanical actuation to magnetic actuation. With magnetic actuation, tolerances are less strict. With shorter length, more cilia can be inserted into the same chip area. In addition, the orientation of the cilia is in axial alignment as opposed to the first generation in which the cilia are interwoven to increase resolution. The 3rd generation sensor, not pictured, shares the same structure as the second, but the overall size is 1mm x 4mm.

The placement of the piezoresistor was determined by finite element modeling and analysis (FEM-A) and was chosen by determining the portion of the beam with the maximum change in stress. The electronics of the sensor design evolved to interface correctly with the neural network of the robotic cricket, minimize power, and minimize computational demands on the neural network. Both topics are discussed in the following section.

2.2 Theory of Operation

2.2.1 Introduction

As stated previously, piezoresistivity is a material property regarding bulk resistivity changing with external mechanical stresses. The change in resistivity is calculated by using FEM to analyze the mechanical stresses in the piezoresistors caused by residual stress and by the external bending of the cantilever beam. The change in voltage in the polysilicon wheatstone bridges is then calculated using equations that characterize the change in resistance due to applied stress.

2.2.2 Stress Analysis

The stress states of the beams were analyzed using MemCAD,²¹ a finite element modeling and analysis software package. The states analyzed were the two limit conditions: 1) no external stress applied to the beam and 2) the maximum flex condition (i.e. when the beam comes in contact with the surface of the wafer). Under no external stress, the beam is free to curl due to residual stress of the layers. During the fabrication of the MEMS device, myriads of stresses are introduced from both thin film deposition and coefficient of thermal expansion (CTE) mismatch. While MemCAD is an effective tool for direct mechanical modeling, it is unable to calculate directly the stress state produced from the combination of these stresses. Accurate prediction of the cilia, however, was achieved by substituting a residual thermal stress for the mechanical and structural stresses. Using this approach, the cilia were evaluated using an applied temperature of 117 K. Previous experimental work by Sitaraman Iyer et al in “Analysis of Temperature-Dependent Residual Stress Gradients in CMOS Micromachined Beams” determined the temperature value. In their experimental work, several beams of varying composition were fabricated and released. Using the sample line option in the MemCAD Visualizer, stress values could be extracted from points on the graphical representation of the beam and inserted into a spreadsheet. The maximum flex condition was achieved by displacing the tip of the curled beam model such that the tip of the beam was at zero z-axis position (in-plane with the wafer surface). Again, the stress values were extracted. The stress values extracted were the stresses corresponding to the principle axes and the von Mises stress.

$$\sigma' = \left[\frac{(\sigma_1 - \sigma_2)^2 + (\sigma_2 - \sigma_3)^2 + (\sigma_1 - \sigma_3)^2}{2} \right]^{\frac{1}{2}}$$

Equation 1. von Mises Stress Calculation²²

The von Mises stress, σ' , is defined by *Equation 1* where σ_1 , σ_2 , and σ_3 are stresses along the principal axes. The change in von Mises stress, or effective stress, for the 1st and 2nd generation designs are shown in Figure 14 and Figure 16, respectively. The holes in the beams as observed in Figure 15 and

Figure 17 are for release purposes. The holes are not included in the simulations due to convergence failures.

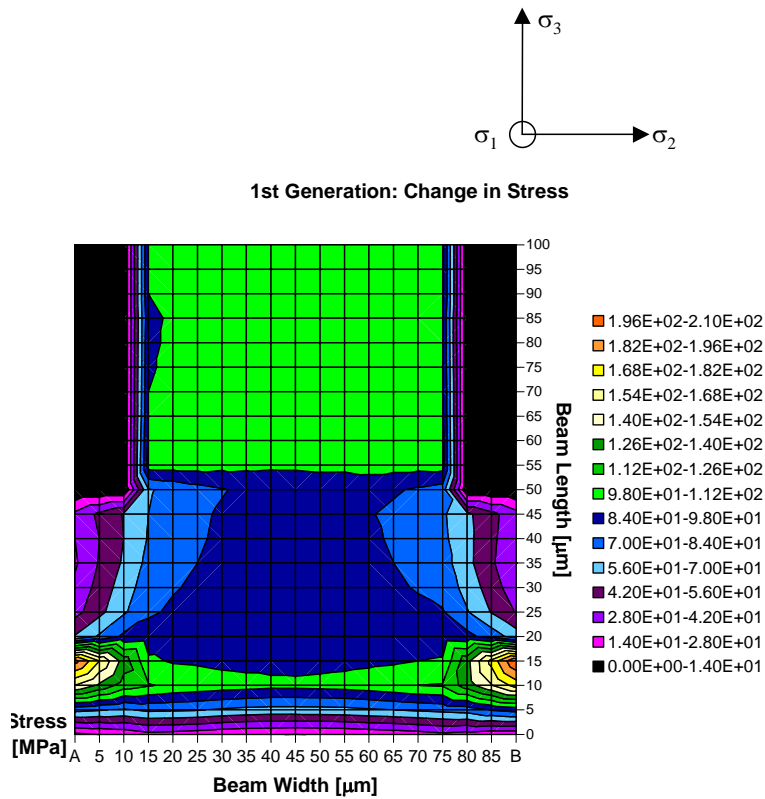


Figure 14. Change in von Mises Stress [1st generation]

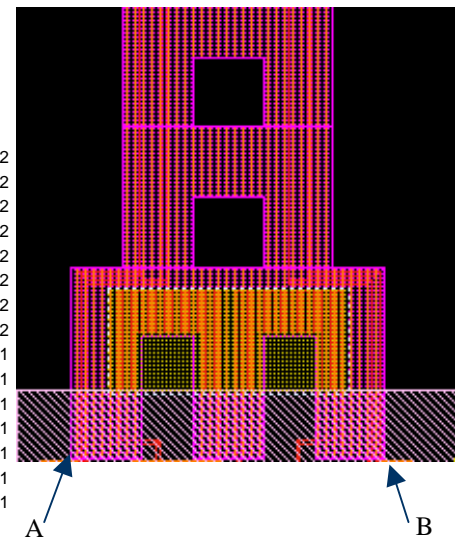


Figure 15. Layout of Cilia Anchor [1st generation]

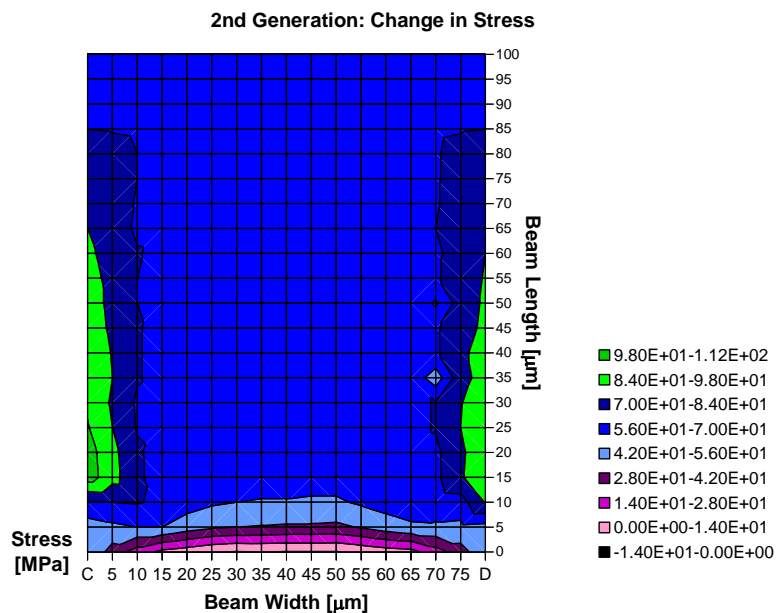


Figure 16. Change in von Mises Stress [2nd generation]

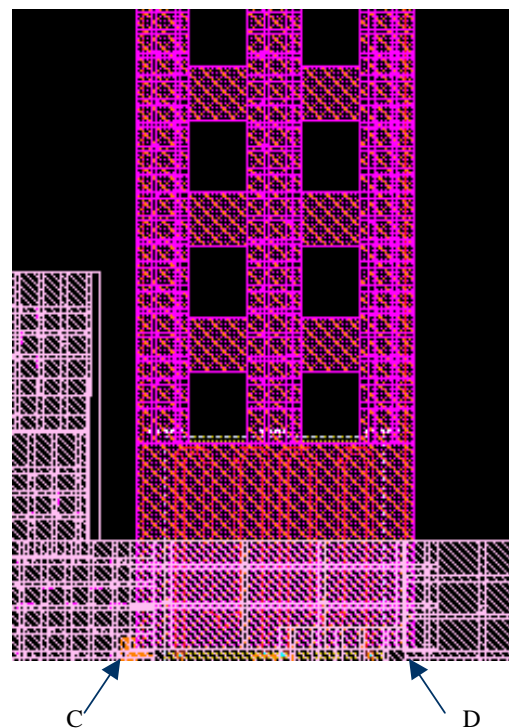


Figure 17. Layout of Cilia Anchor [2nd generation]

In Figure 15 and Figure 17, the orange serpentine line denotes the polysilicon resistor. In the first design judging by the von Mises stress, MemCAD simulations reveal that the resistor would have been better suited farther from the anchor of the beam. However, in the second design, the resistor was more optimally placed.

The beams were modeled with a square of polysilicon at the anchor as opposed to the serpentine used in the layout. This was to enable extraction of the sample points from the Visualizer in MemCAD. Seven sample lines, each with 20 sample points, were spaced every 10 μm from the edge of the anchor. Of the three principle axes, the longitudinal axis is of primary concern for three reasons. The first is that the axis in parallel with the width of the beam experiences negligible stress. The second is that the axis in parallel with the thickness of the beam is not meshed enough to provide an accurate stress value. Third, for a first order approximation, the stress parallel to the thickness of the beam has little effect on piezoresistivity of the polysilicon.²³ The averages of the longitudinal stress values are listed in Table 2.

Table 2. Average Stress Values for 1st and 2nd Generation Beams

Average Longitudinal Stress (σ_3) [MPa]	1 st Beam Generation	2 nd Beam Generation
No external stress applied	36.4	15.8
External stress applied	17.4	11.1

As expected the longitudinal stress becomes less tensile as the beam is flexed from curled to flat, since the polysilicon layer is on the bottom of the beam. Due to the non-uniformity of the stress through the thickness of the beam, the stress values extracted are expected to be in error by ± 3 MPa. In the following section, the stress component values will be used to calculate the expected change in resistance for each beam design.

2.2.3 Piezoresistivity and Polysilicon

The piezoresistive effect, using polysilicon piezoresistors in a wheatstone bridge, is used to sense the motion of the cilia. To determine the expected change in voltage at the outputs of the wheatstone bridge, the change in resistance due to applied stress must be calculated. However, the mechanical properties that are used to determine the change in resistance vary with deposition conditions. For the most part, though, the mechanical properties are similar to those of silicon.²⁴ Therefore, mechanical properties of silicon will be used to estimate an overall expected change in resistance for an average applied stress. The particular mechanical properties of interest are the parallel and perpendicular coefficients of piezoresistivity, π_{\parallel} and π_{\perp} , respectively. The fractional change in resistivity can be calculated to a first order degree by the following equation, where σ_{\parallel} and σ_{\perp} are stress components in the parallel and perpendicular to the direction of current flow in the resistor.

$$\frac{\Delta\rho}{\rho} = \pi_{\parallel}\sigma_{\parallel} + \pi_{\perp}\sigma_{\perp}$$

Equation 2. 1st Order Equation of the Fractional Change in Resistivity

The parallel and perpendicular stress components used to calculate the fractional change in resistivity were determined by MemCAD simulations and are listed in Table 3, where σ_{\parallel} and σ_{\perp} correspond to σ_3 and σ_2 , respectively.

Table 3. Coefficients of Piezoresistivity for Silicon for n- and p-type {100} wafers and Doping Levels below 10^{18}cm^{-3} ²²

Doping type	Orientation	π_{\parallel} [$10^{-13}\text{m}^2/\text{N}$]	π_{\perp} [$10^{-13}\text{m}^2/\text{N}$]
p-type	<100>	0	0
	<110>	72	-65
n-type	<100>	-102	53
	<110>	-32	0

Table 4. Fractional Change in Resistivity for Sample Coefficients of Piezoresistivity

Silicon parameters	Fractional change in resistivity $\Delta\rho/\rho$			
	1 st generation beam		2 nd generation beam	
	no external stress $\Delta\rho_1/\rho$	External stress $\Delta\rho_2/\rho$	No external stress $\Delta\rho_1/\rho$	External stress $\Delta\rho_2/\rho$
p-type, <100>	0	0	0	0
p-type, <110>	.0026	.0012	.0011	.0008
n-type, <100>	-.0037	-.0018	-.0016	-.0011
n-type, <110>	-.0012	-.0006	-.0005	-.0004

Table 5. Calculated Fractional Change in Resistivity

Silicon parameters	Overall fractional change in resistivity $(\Delta\rho_1-\Delta\rho_2)/\rho$	
	1 st generation beam	2 nd generation beam
p-type, <100>	0	0
p-type, <110>	.0014	.0003
n-type, <100>	-.0019	-.0005
n-type, <110>	-.0006	-.0001

The calculated values for the fractional change in resistivity listed in Tables 4 and 5 are for the ideal case and will be used to verify the stress values calculated by MemCAD simulations by providing a calculated fractional change in resistivity to be compared to experimental results. The non-idealities that are not included in this calculation by using coefficients of piezoresistivity for silicon are the non-uniform crystal orientations, and the effects of the grain among others. These non-idealities are expected to decrease the magnitude of the fractional change in resistivity.

2.2.4 Summary

Values for fractional change in resistivity have been calculated using silicon coefficients of piezoresistivity and FEM to determine stress components for each beam design. Once the cilia are tested, the method of estimating fractional change of resistivity will be evaluated.

2.3 Cantilever Beam Composition

Composition of the beam determines the radius of curvature along the length of the beam. Minimizing the radius of curvature of the beam maximizes the out-of-plane displacement for a given length, and thereby decreases beam area for out-of-plane displacement. Therefore, beam composition is chosen to minimize radius of curvature. Previous experiments determined that a beam composed of metal 1 and metal 2 in the .5 HP CMOS process has a radius of curvature of 1 mm, which is the smallest for any combination of the available layers.²⁵ Out-of-plane displacement (Z) for a given length (L) and radius of curvature (λ) can be determined by Figure 18 and Equation 3.

For each generation, the out-of-plane tip displacement was calculated. Once the beams were fabricated and released, the out-of-plane displacement was measured. The

calculated and measured out-of-plane tip displacement is shown in **Table 6**. The measured out-of-plane displacement was obtained by using the fine focus micrometer on the probe station microscope. The data sets differ by less than 3%, verifying that the methods for both calculating and measuring out-of-plane displacements are satisfactory.

$$\theta = \frac{L}{2\pi\lambda} * 360$$

$$L' = \sqrt{2\lambda^2 - 2\lambda^2 \cos \theta}$$

$$\phi = \frac{\theta}{2}$$

$$Z = L' \sin \phi$$

Equation 3. Calculating Out-of-Plane Displacement

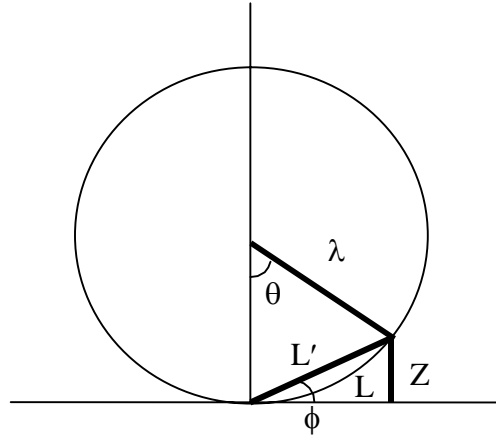


Figure 18. Calculating Beam Curl

Table 6. Lengths and Out-of-Plane Displacements

Generation	Length (L) [μm]	Calculated Out-of-Plane Tip Displacement (Z) [μm]	Measured Out-of-Plane Tip Displacement (Z) [μm]
1	3075	2000	1975
2	848	339	331
3	560	153	Not released

2.4 Integrated Signal Conditioning

2.4.1 Introduction

Without on-chip signal conditioning, the alternatives such as circuit boards or modification of the neural network chip would increase weight and size of the robot or increase the complexity of the neural network, respectively. The outputs of the sensing

elements of the cilia are expected to be quite small, in the range of tens of millivolts. Therefore, the minimum signal conditioning effort is to amplify the outputs. How, when, and which cilium to amplify were determined by an iterative design process described in the following sections.

2.4.2 Wheatstone Bridge

A wheatstone bridge composed of polysilicon piezoresistors is used to sense cantilever beam bending. An advantage of the wheatstone bridge is that it is insensitive to temperature. However, resistor mismatch is a significant problem that causes a non-zero dc offset at the output of the polysilicon wheatstone bridges. Since polysilicon resistors may deviate from their nominal value by 10 to 20%, the offset is considerable. More importantly, residual stress is very different between the mechanically released and the anchored resistors. Therefore, the resistance offset can be even larger than 20%. Two steps were taken in the third design to reduce resistor mismatch. First, the resistors were laid out in a distributed manner. See Figure 19 for the schematic of the resistor layout and Figure 20 for an illustration of the layout.

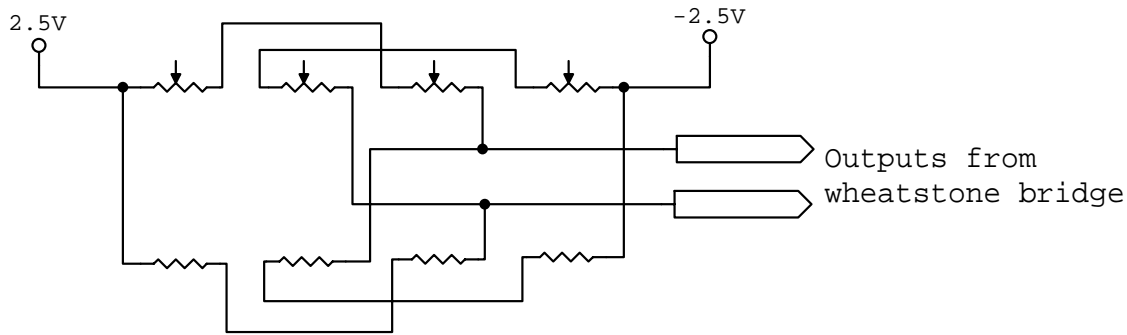


Figure 19. Schematic of Resistor Layout

Essentially, two resistors for each resistor were created. The resistors were connected in series, each to the alternating resistor in the layout. This reduces changes in resistance due to spatial separation on the wafer surface. Second, a pseudo-cilium was designed. A pseudo-cilium is a short cantilever beam, just long enough for the placement of the resistors, which is released but not actuated. See Figure 20 for an illustration. The resistors in the wheatstone bridge that are fixed in value are located in the pseudo-cilium. In this way, all resistors experience the curl of the beam and change in stress and resistance caused by the release of the cantilever beam.

2.4.3 Multiplexing

The signal conditioning of the 1st generation design used multiplexing to select the output of an individual sensing element to be amplified. With multiplexing, each cilium has an address that enables an output line of a digital encoder, which then closes switches to power lines and to the amplifier circuit connected to the activated cilium. The decoder line in the schematic is specific to the individual cilium. See Figure 21 for the decoder. See Figure 22 for a schematic of the switches that enable outputs from the cilia. The

outputs of the wheatstone bridge are labeled “Opamp” and are the inputs to an operational amplifier as shown in Figure 23.

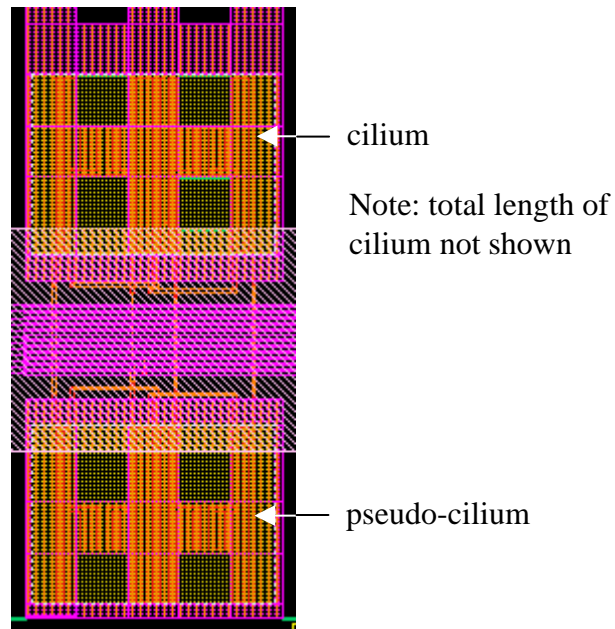


Figure 20. Layout of Cilium with Pseudo-cilium

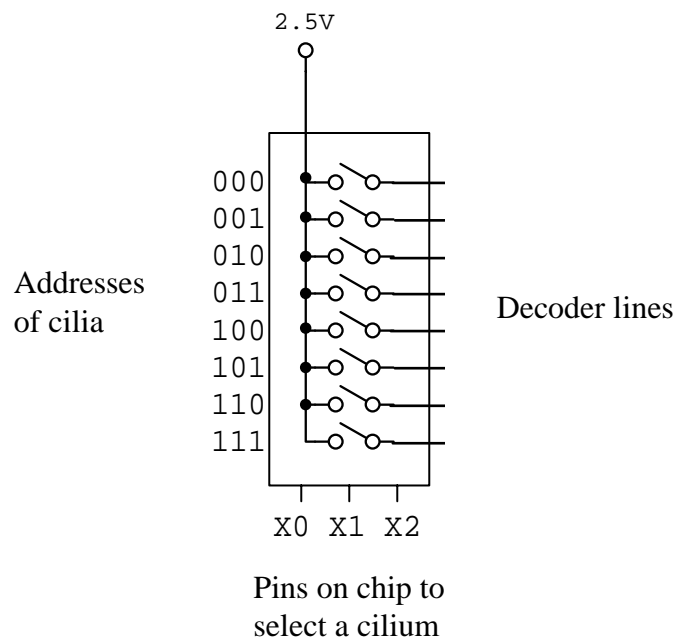


Figure 21. Decoder for 1st Generation JAS

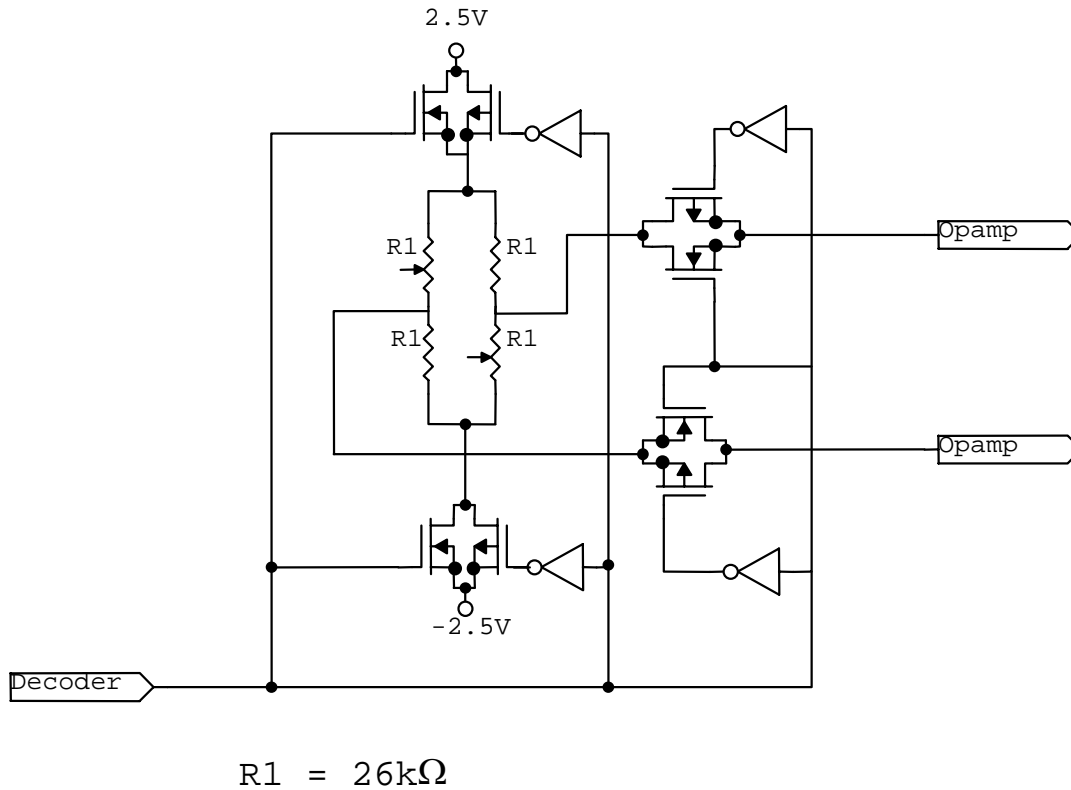


Figure 22. 1st Generation JAS – Individually Addressed Cilium

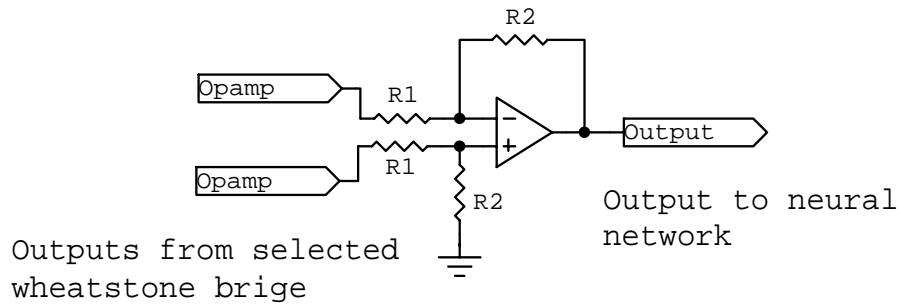


Figure 23. Amplification Circuit for 1st Generation JAS

Multiplexing is a low power solution. At a single instance of time, the only active circuitry is the digital encoder, a wheatstone bridge, and the operational amplifier (see Table 7). However, while the output is continuous, it corresponds to only one of the sensing elements.

Table 7. Power Consumption for Individual Analog Components of 1st Generation

Analog Component	Power Consumption (± 2.5 V Power Supply) [mW]
Wheatstone Bridge	.24
Operational Amplifier	50

Also, the interface to the neural network is more complex due to the additional input lines to the digital encoder. The number of input lines is grows as $\log_2(\text{number of cilia})$. See **Table 8** for the list of mandatory pins and their functions.

Table 8. 1st Generation Pins and Functions

Pins	Function
Vdd, Vss, GND	± 2.5 Power Supplies, GND
X0,X1,X2	Inputs to decoder – 3 inputs results in 8 decoder lines
Vout	Output of the sensor

2.4.4 Summing

In order to decrease the complexity of the interface and provide a continuous output that combines the outputs of all sensing elements, the amplification of the sum of the wheatstone bridges was employed in the 2nd generation JAS as shown in Figure 23. Due to the small signal output from the wheatstone bridges, the signal is preamplified before summing (see Figure 24). The voltage offset introduced by the preamplification is cancelled by differencing the preamplifier outputs from the paired cilia. Figure 25 contains the summing circuit schematic.

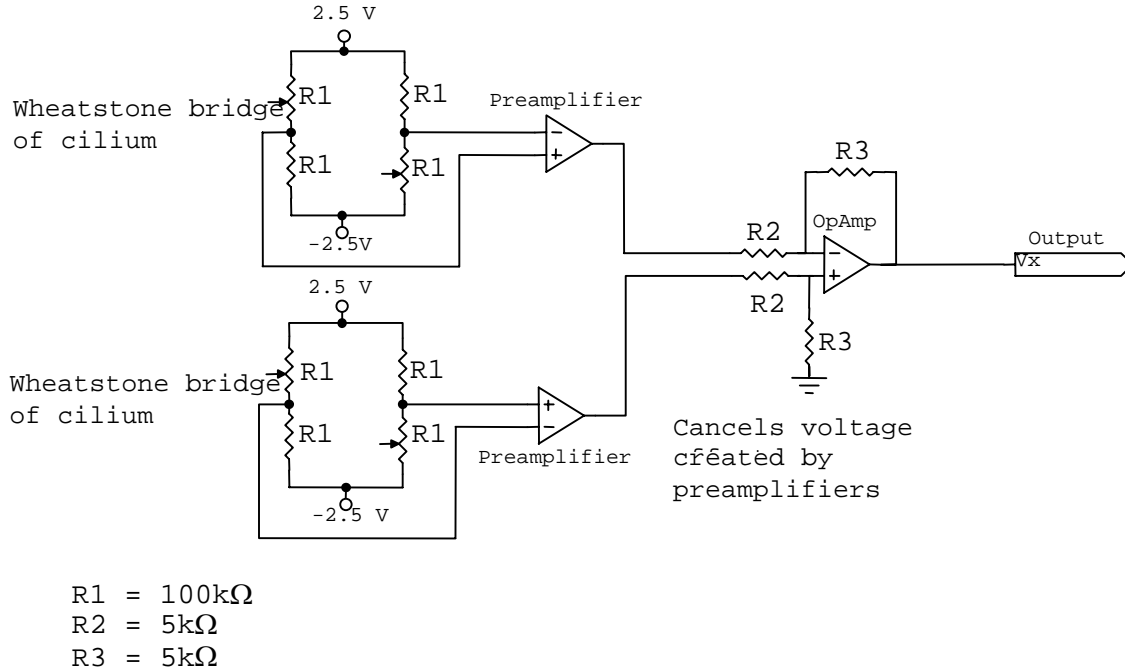


Figure 24. Wheatstone Bridges with Preamplification and Voltage Offset Cancellation

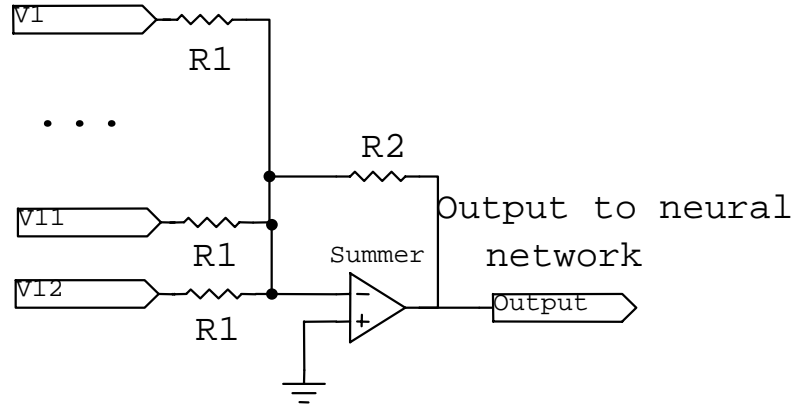
$$V_x = \{[(\Delta V_1)P + V_{\text{offset}}] - [V_{\text{offset}} - (\Delta V_2)P]\}G$$

$$V_x = [\Delta V_1 + \Delta V_2]PG$$

Equation 4. Calculating the Output of Figure 24

Cancellation of the offset is described by Equation 4; where V_x is the output of amplification of a pair of sense elements, ΔV_1 and ΔV_2 are the outputs of the wheatstone bridges, V_{offset} is the resultant offset caused by the preamplifier, P is the gain of the preamplifier, and G is the gain of the difference circuit. The offset of each pair of preamplifiers is assumed to be constant since the preamplifiers are adjacently located on the chip in addition to having their current sources driven by the same current mirror.

Outputs from wheatstone bridges and amplifiers



$$\begin{aligned} R1 &= 4\text{k}\Omega \\ R2 &= \text{off-chip} \end{aligned}$$

Figure 25. Summing Circuit Schematic

While this strategy fulfills the continuous output request, the power consumption is much higher than desired. All circuits are on continuously. For each pair of cilia, two differential pair preamplifiers, an operational amplifier, and two wheatstone bridges are powered in addition to the operational amplifier used for summing. Table 9 lists components and power consumption.

Table 9. Power Consumption for the 2nd Generation

Component	Power Consumption (± 2.5 V Power Supply) [mW]	Number of Instantiations	Total Power Consumption [mW]
Wheatstone Bridge	.0625	24	1.5
Preamplifier (no load)	.185	24	4.44
Operational Amplifier (voltage offset cancellation; no load)	1.7	12	20.4
Operational Amplifier (summing circuit)	50	1	50

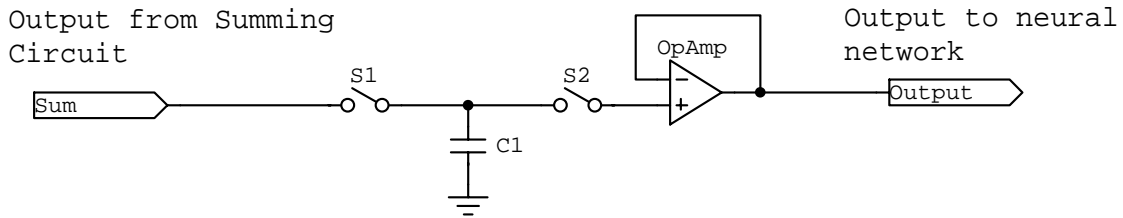
However, the pin count is reduced as shown in Table 10.

Table 10. 2nd Generation Pins and Functions

Pins	Function
Vdd, Vss, GND	Power supplies [± 2.5 V] and Ground
Vout	Output of sensor

2.4.5 Sample/Hold

To reduce the power consumption of the 2nd generation JAS, a sample/hold circuit was introduced in the 3rd generation JAS. The clocking of the sample/hold circuit is on-chip and there is an override mechanism to clock off-chip. With a sample/hold circuit, the output is continuous, while portions of the circuitry are powered down to minimize power consumption, as shown in Figure 26. The power consumption of components in the 3rd generation device is listed in Table 11.

**Figure 26. Sample/Hold Circuit Diagram****Table 11. Power Consumption for the 3rd Generation**

Analog Component	Power Consumption (± 2.5 V Power Supply) [mW]	Number of Instantiations	Percentage of clock cycle enabled	Total Power Consumption [mW]
Wheatstone Bridge	.125	24	100	3
Preamplifier	.185	24	50	2.22
Operational Amplifier (voltage offset cancellation; no load)	1.7	12	50	10.2
Operational Amplifier (summing circuit)	50	1	25	12.5
Operational Amplifier (sample/hold)	50	1	100	50

2.4.6 Summary

Communication with CWRU indicated that the most desirable joint angle sensing solution would be one that produced an identifiable signal that corresponded to a specific joint angle measurement. In the effort to achieve this, power consumption was increased. To reduce the power consumption a sample/hold circuit was added. Power was not

reduced significantly. However, as the minimum updating frequency required is 1 kHz, the percentage of time that most of the circuitry is on can be reduced significantly by decreasing the duty cycle percentage and the clocking frequency.

2.5 Summary

This section has described the design of the joint angle sensor, including the cantilever beam, signal conditioning, and the expected output of the sensor. Verification is the following step in the design process.

3. EXPERIMENTATION

3.1 Introduction

Experimentation comprises characterizing the main components of the sensor, the operational amplifier used in the first and second generation, and the cilia. For the 1st generation sensor, the decoder and pass gates were also tested for functionality. Due to a design error of the cilia of the 2nd generation, the polysilicon resistors are not uniformly released, causing some cilia to be under-etched and others to be overetched. Therefore, the complete sensor design could not be tested. The cilia response was tested where possible. The 3rd generation has not been released and therefore not tested.

3.2 Operational Amplifier

A component of the JAS that was implemented and requires testing to verify operating parameters is the operational amplifier used in all versions of the joint angle sensor. It is a low-voltage two-stage amplifier with a rail-to-rail common-mode input range and rail-to-rail class-AB output stage. The first stage topology is an n-type folded cascode in parallel with a p-type folded cascode. The topology was based on a design found in the *Hewlett Packard Journal*.²⁶ Other specifications of interest are listed in Table 13.

The design process started with sizing the transistors for maximum gain based on hand calculations. The overall design was simulated using Hspice. Once the sizes of the transistors were optimized, the circuit was laid out in Cadence. Then, the netlist for the Hspice simulation was extracted from the layout of the operational amplifier and simulated. The following are the resultant graphs of the gain and the phase plots. The operational amplifier was fabricated in two different processes, AMS .6 μm CMOS and HP .5 μm CMOS. The open loop transfer curves are shown in Figures 27 and 28. A characterization of the simulated operational amplifier is summarized in Table 12.

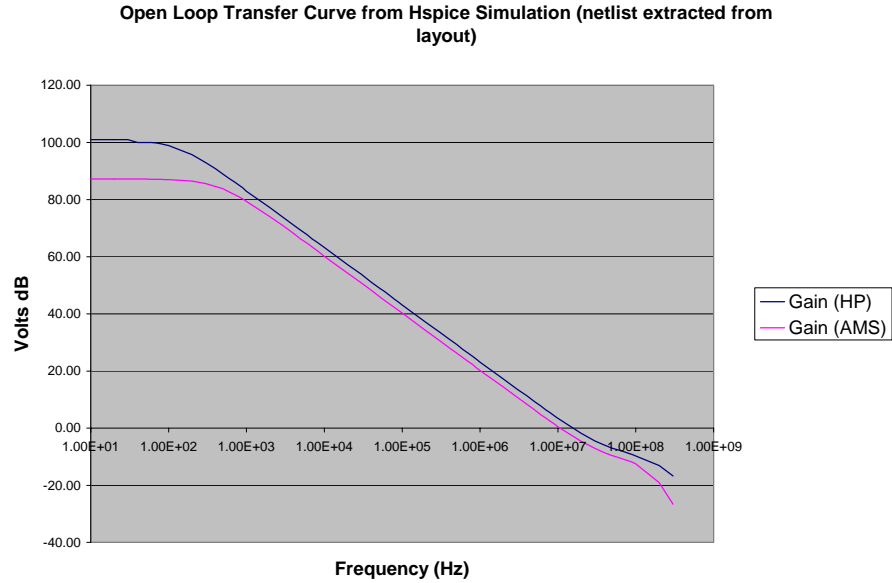


Figure 27. Open Loop Transfer Curve for Operational Amplifier

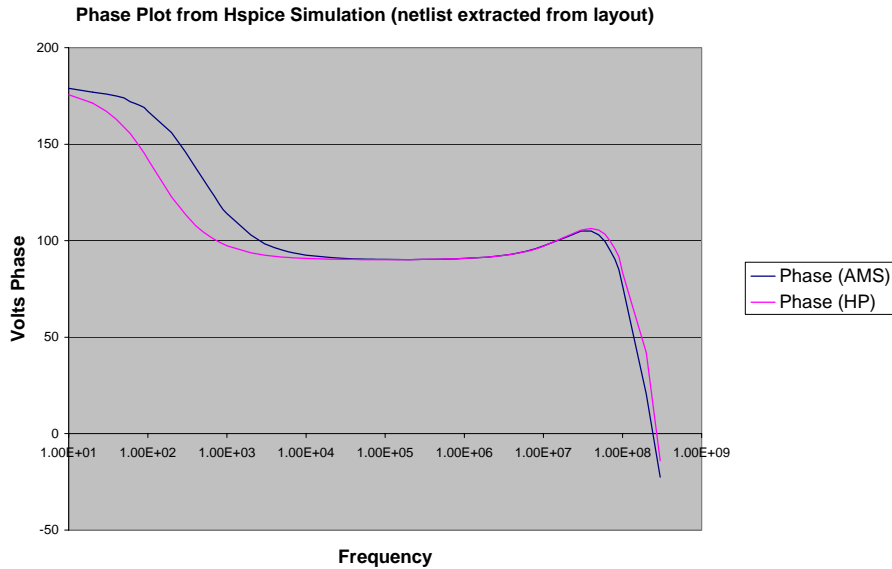


Figure 28. Phase Plot from Hspice Simulation

Process	dc Open Loop Gain [dB]	3-dB point [Hz]	Unity Gain Frequency [MHz]
HP .5 μ m CMOS	101	128	10
AMS .6 μ m CMOS	87	446	10

Table 12. Characterization of the Operational Amplifier from Simulation

The sensors were wire-bonded to 40-pin packages and mounted on a protoboard. The circuit was wired as a unity gain buffer. Power was supplied by an HP E3630A power supply (-2.5 V, 2.5 V). Test signals were supplied with an HP 33120A function/arbitrary

waveform generator. The output of the circuit was sensed by an HP 54645D mixed signal oscilloscope and/or an HP 4395A network/spectrum/impedance analyzer. The following table lists the experiments conducted and results obtained.

Parameter	Target	Result
Input offset voltage	N/A	3 – 4 mV
Output voltage range	$AV_{ss} + .2 \leq V_{out} \leq AV_{dd} - .2$	$-2.125 \leq V_{out} \leq 2.125$
Common-mode input range	$AV_{ss} \leq CMIR \leq AV_{dd}$	$-2.1 \leq CMIR \leq 2.1$
Cut-off frequency (unity gain)	5 MHz	6 MHz
Single-supply operation	$2.7 \leq AV_{dd} \leq 3.6$	$3 \leq V_{dd} \leq 5$
Low quiescent power consumption	1 mA	10 mA
Slew Rate	$1 \text{ V}/\mu\text{s} \leq SR \leq 5 \text{ V}/\mu\text{s}$	$10 \text{ V}/\mu\text{s} \leq SR \leq 34 \text{ V}/\mu\text{s}$

Table 13. Target and Resultant Parameters

In general, the result values are comparable to the target values except for quiescent current and slew rate. Future designs could optimize the quiescent current; however, as slew rate is proportional to the current in the output stage, a reduction in current would also reduce the slew rate.

3.3 Cilia

The response to mechanical deformation of the cilia was generated by collecting data from a wafer probing station. Prior to the experiment, the chips were wirebonded to a ceramic 40-pin package such that the sensor was exposed. The package was mounted to a protoboard and the protoboard was held in place on the probe station with vacuum. Power and ground supplies were connected along with probes to the outputs of the cilia. The cilia of the 1st generation were tested by first enabling a specific cilium with its corresponding address. The cilia of the 2nd generation did not require addressing. A micromanipulator probe tip was used to bend the cilia. Using the micrometer head, the probe tip was positioned directly above the end of the cilium. Next, the probe tip was lowered under microscope observation until it just touched the cilium. At this point, the initial position was read from the micrometer head. The probe was then lowered controlled amounts and the output of the wheatstone bridges was tabulated. The resultant graphs are shown below in Figure 29 and Figure 30.

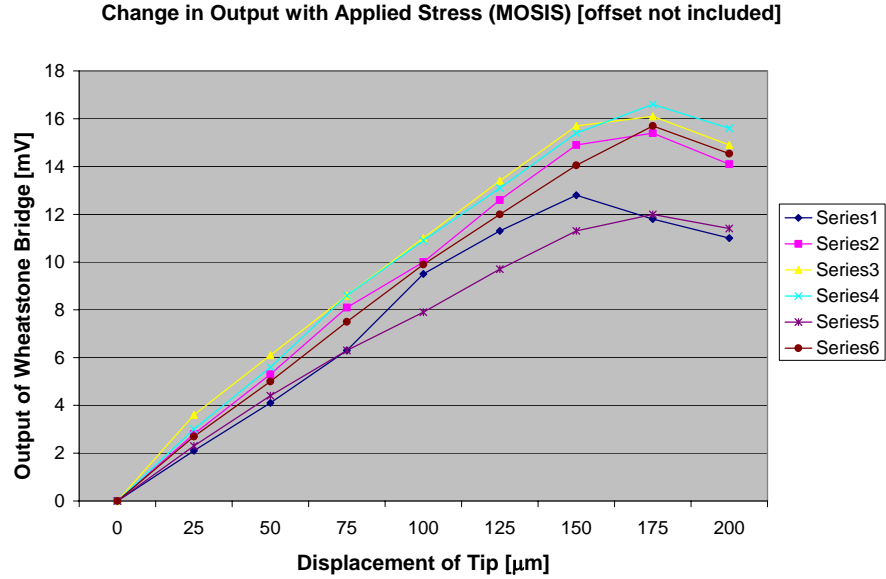


Figure 29. Cilia Characterization – 1st Generation JAS

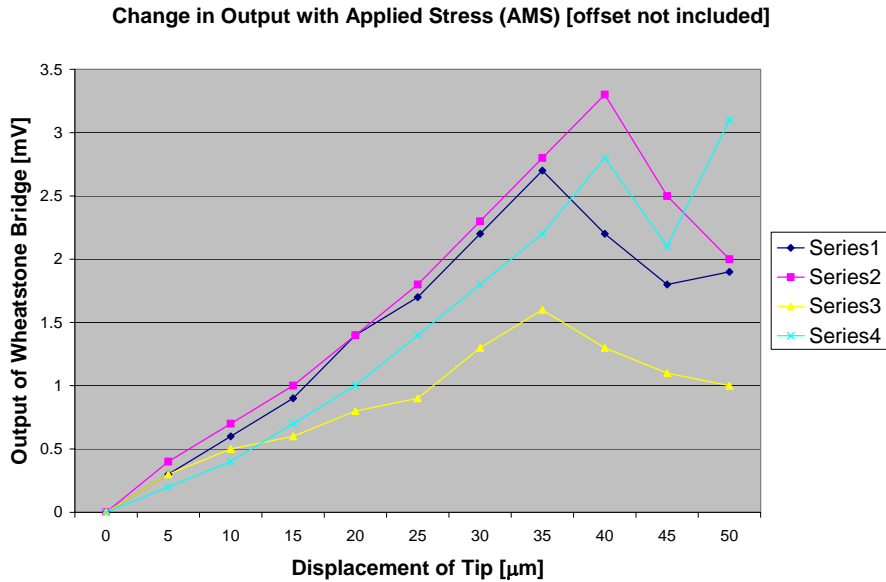


Figure 30. Cilia Characterization – 2nd Generation JAS

Due to the longer length of the cilia of the 1st generation JAS, the cilia tips could be pressed farther down which accounts for the different x-axis scales. The change in outputs of the Wheatstone bridges with increased stress in Figure 29 indicates that the decoder and pass gates are functional. Observation of the slopes in the graphs in Figure 29 and Figure 30 shows that the slopes level off and actually change direction. It is hypothesized that part of the beam eventually hits the bottom of the trench and thereby lessens the stress experienced at the anchor of the beam where the polysilicon piezoresistors are located. Based on this hypothesis, the range of operation of motion in the z-axis for the 1st generation and 2nd generation cilia is between 0 and 150 μm and

between 0 and 45 μm , respectively. Direct comparison of the two different beams is precluded by the fact that two different fabrication processes and two different designs were used.

The average maximum fractional change in resistivity obtained from experiment is .15% for the 1st generation cilia and .026% for the 2nd generation cilia. However, the beam in the experiment was bent past the plane of the surface of the sensor and hit the bottom of the trench unlike the simulated beam. The beams were simulated again in MemCAD but did not converge. Therefore, assuming the trench is 20 μm deep, the normalized average maximum fractional change in resistivity is .13% for 1st generation and .016% for 2nd generation. The simulations of the cilia in MemCAD resulted in a maximum expected change of .14% for the 1st generation cilia and .03% for the 2nd generation cilia using silicon coefficients of piezoresistivity. The experimental data seems to support that the polysilicon is p-type and that the transverse stress is negligible. Assuming this correct, a piezoresistive coefficient in the longitudinal direction can be calculated. The longitudinal coefficients of piezoresistance in Table 14 can be calculated from Equation 5.

Beam generation	$\pi [10^{-12}\text{m}^2/\text{N}]$
1 st (HP .5 μm)	73.8
2 nd (AMS .6 μm)	25.5

Table 14. Longitudinal Coefficients of Piezoresistivity for AMS .6 μm and HP .5 μm CMOS Processes

$$\begin{aligned}\frac{\Delta\rho_1}{\rho} &= \pi_{||}\sigma_{||_1} \\ \frac{\Delta\rho_2}{\rho} &= \pi_{||}\sigma_{||_2} \\ \frac{\Delta\rho_1 - \Delta\rho_2}{\rho} &= \pi_{||}(\sigma_{||_1} - \sigma_{||_2})\end{aligned}$$

Equation 5. Calculating the Longitudinal Coefficient of Piezoresistivity

4. DISCUSSION

The following is a brief discussion on the joint angle sensor project. Issues such as resistor mismatch and MemCAD simulation validity are covered. Also, the three designs are briefly reviewed and compared. In addition, future work is explored.

4.1 Sources of Error

4.1.1 Resistor Mismatch

Resistor mismatch is likely the greatest problem with the joint angle sensor, especially with the summing approach. The dc offset at the output of the wheatstone bridges is hundreds of millivolts, while the output component due to external bending of the cilia is at most tens of millivolts. Amplification of the signal is limited by the dc offset. Too much amplification will saturate the output of the amplifier such that the change in voltage due to external stress is not detectable. The first and second generations of the joint angle sensor do not adequately reduce the effect of resistor mismatch. The third generation does attempt to reduce the mismatch through use of pseudo-cilia and distributed resistors, but this is unlikely to eliminate resistor mismatch.

4.1.2 MemCAD Simulations

MemCAD simulations are useful, but the method for extracting stress values is flawed. A sample line of 250 maximum points can be used to extract stress values from the graphic of the beam in the Visualizer. However, stress is a volumetric state that is not accurately obtained using a 2-D line. In addition, placement of the line is not rigorous. No coordinates indicate that the line has been placed in the same place as it was placed in other beam simulations, a particular problem especially in regard to placement of the line in the z-axis (through the thickness) of the beam, which hinders accuracy and repeatability. MemCAD uses ABAQUS²⁷ to calculate stress values. The output file from ABAQUS has the stress values listed by node. It would have been much wiser to use MemCAD to set up and run the simulation and then use the ABAQUS output file to determine the stress.

4.2 Comparison of 1st Generation and 2nd Generation

This section briefly reviews and compares the three joint angle sensor designs. The 1st generation has a decoder that accesses and amplifies the output of each cilium individually. The 2nd generation sums the amplified outputs of each of the wheatstone bridges. The 3rd generation JAS adds a sample/hold circuit to the circuitry of the 2nd generation to reduce power consumption. The power consumption of the 1st generation is significantly less than the 2nd generation. The 3rd generation can be optimized to reduce power consumption, but the result of the optimization can at best match the power consumption of the 1st generation. Increased power consumption is the price for continuous output and simplified interface that were specified by Case Western Reserve University. All the designs are limited by the resistor mismatch, but the 1st generation is the least hindered.

4.3 Future Work

The work to be completed is the integration of the sensor and the robot, which includes using magnetic actuation of the cilia. To complete the integration, a final design will be submitted for fabrication. The electronics and chip topography (i.e. dimensions, number of cilia, dimensions of cilia) will remain the same as the third generation with errors

removed. The investigation of the magnetic actuation also remains. Some parameters to be determined are the material type, a soft magnetic material such as permalloy (NiFe) or a hard magnetic material such as cobalt platinum (CoPt), the thickness of the layer, and the process for depositing the magnetic layer.

5. CONCLUSIONS

A joint angle sensor using MEMS cilia has been designed and fabricated. The polysilicon piezoresistors used to sense motion of the cilia have been tested; and using MemCAD to obtain stress values, coefficients of piezoresistivity have been obtained for both AMS and HP fabrication processes. A low-voltage rail-to-rail common-mode input, rail-to-rail output operational amplifier has been designed to amplify the output of the polysilicon wheatstone. The operational amplifier performs closely to target parameters except for greater quiescent current consumption. Further iterations of the design will be done to remove layout wiring errors to complete full system testing.

6. BIBLIOGRAPHY

- ¹ M.C. Birch, R.D. Quinn, et al., "Design of a Cricket Microrobot," International Conference of Robotics and Automation, San Francisco, 2000.
- ² MicroMo Electronics, Inc. www.micromo.com
- ³ Newark Electronics Catalog, v. 116, 1998, pp. 668 – 726.
- ⁴ *The Pressure Strain and Force Handbook*, Omega Engineering, Inc., 1995.
- ⁵ V.A. Gridchin, V.M. Lubimsky, M.P. Sarina, "Piezoresistive properties of polysilicon films," *Sensors and Actuators A*, vol. 49, 1995, pp. 67 – 72.
- ⁶ E.R. Kandel, J.H. Schwartz, T.M. Jessell, *Principles of Neural Science*, 3rd edition, Norwalk: Appleton & Lange, 1991.
- ⁷ V.G. Dethier, *The Physiology of Insect Senses*, New York: John Wiley & Sons, Inc., 1963.
- ⁸ Sir Vincent B. Wigglesworth, *Insect Physiology*, New York: John Wiley & Sons, Inc., 1966.
- ⁹ R.F. Chapman, *The Insect: Structure and Function*, New York: American Elsevier Publishing Company, Inc., 1969.
- ¹⁰ X. Zhu et al., "Characterization of Silicon Isotropic Etch by Inductively Coupled Plasma Etch in Post-CMOS Processing," in *Proc. of the IEEE Micro Electro Mechanical Systems Workshop (MEMS 2000)*, pp. 568 – 573.
- ¹¹ G.K. Fedder et al., "Laminated High-Aspect-Ration Microstructures in a Conventional CMOS Process," in *Proc. of the IEEE Micro Electro Mechanical Systems Workshop (MEMS '96)*, pp. 13 – 18.
- ¹² E. Peiner, D. Scholz, A. Schlachetzki, P. Hauptmann, "A micromachined vibration sensor based on the control of power transmitted between optical fibres," *Sensors and Actuators:A*, vol. 65, 1998, pp. 23 – 29.
- ¹³ H.P Lang, et al, "The Nanomechanical NOSE," in *Proc. of the IEEE Micro Electro Mechanical Systems Workshop (MEMS '99)*, 17 – 21 Jan 1999, pp. 9 – 13.
- ¹⁴ M. Ito, E. Yamamoto, et al., "Compound-Cavity Tactile Sensor Using Surface-Emitting Laser," *Sixth International Symposium on Micro Machine and Human Science*, 1995, pp. 83 – 88.
- ¹⁵ S.M. Sze, *Semiconductor Sensors*, New York: John Wiley & Sons, Inc., 1994.
- ¹⁶ S.S. Lee, R.P. Ried, and R.M. White, "Piezoelectric Cantilever Microphone and Microspeaker," *Journal of Microelectromechanical Systems*, vol. 5, no. 4, Dec 1996, pp. 238 – 242.
- ¹⁷ W.-s Choi, J.G. Smits, and G.W. Woodruff, "A Tactile Sensor for the Determination of Object Positions," *IEEE 1991 Ultrasonics Symposium Proceedings*, 1991, pp. 327 – 30.
- ¹⁸ T.R. Albrecht, S. Akamine, et al, "Microfabrication of cantilever styli for the atomic force microscope," *Journal of Vacuum Science Technology A*, vol. 8, no. 4, July/August 1990, pp. 3386 – 3396.
- ¹⁹ S. Akamine, T.R. Albrecht, et al, "Microfabricated Scanning Tunneling Microscope," *IEEE Electron Device Letters*, vol. 10, no. 11, November 1989, pp. 490 – 492.
- ²⁰ X. Li, M. Bao, et al, "A micromachined piezoresistive angular rate sensor with a composite beam structure," *Sensors and Actuators*, vol. 72, 1999, pp. 217 – 223.
- ²¹ MEMCAD User Guide, Microcosm Technologies Inc, Cary, NC 27513. <http://www.memcad.com>
- ²² Joseph Edward Shigley and Charles R. Mischke, *Mechanical Engineering Design*, New York: McGraw-Hill, Inc., 1989, p. 245.
- ²³ Laurent Latorre, Yves Bertrand, and Pascal Nouet, "On the use of Test Structures of the Electro-Mechanical Characterization of a CMOS compatible MEMS Technology," *Proc. IEEE 1998 Int. Conference on Microelectronic Test Structures*, vol. 11, March 1998, 177 – 182.
- ²⁴ Nadim Maluf, *An Introduction to Microelectromechanical Systems Engineering*, Boston: Artech House, 2000.

-
- ²⁵ Sitaraman Iyer, H. Lakdawala, G.K. Fedder, and Tamal Mukherjee, "Analysis of Temperature-Dependent Residual Stress Gradients in CMOS Micromachined Beams," MSM 2001, San Diego.
- ²⁶ Derek L. Knee and Charles E. Moore, "General-Purpose 3V CMOS Operational Amplifier with a New Constant-Transconductance Input Stage," *Hewlett-Packard Journal*, August 1997, pp. 114 – 120.
- ²⁷ ABAQUS. Hibbit, Karlsson & Sorensen, Inc. Pawtucket, RI 02860-4847.